Emplacement dynamics of a crystal-rich, highly viscous trachytic flow of the Sancy stratovolcano, France

Jean-Marie Prival, Andrew J.L. Harris, Elena Zanella, Claudio Robustelli Test, Lucia Gurioli, Oryaëlle Chevrel, Jonas Biren

THE GEOLOGICAL SOCIETY OF AMERICA®

Emplacement dynamics of a crystal-rich, highly viscous trachytic flow of the Sancy stratovolcano, France

Jean-Marie Prival[1], Andrew J.L. Harris[1,†], Elena Zanella[2], Claudio Robustelli Test[2], Lucia Gurioli[1], Oryaëlle Chevrel[1], and Jonas Biren[3]

[1]*Université Clermont Auvergne, Laboratoire Magmas et Volcans, CNRS, IRD, OPGC, Campus Les Cézeaux, 6 avenue Blaise Pascal, F-63178 Aubière, France*

[2]*Università degli Studi di Torino, Dipartimento di Scienze della Terra, Via Valperga Caluso 35, 10125 Torino, Italy*

[3]*Université d'Orléans, Institut des Sciences de la Terre d'Orléans, CNRS, BRGM, 1A rue de la Férollerie, F-45071 Orléans, France*

ABSTRACT

Emplacement dynamics of highly viscous, silicic lava flows remain poorly constrained due to a lack of consideration of crystal-rich cases. Emplacement models mostly apply to glassy or microlitic, vesiculated rhyolitic flows. However, crystalline, vesicle-free silicic lava can flow differently. We studied the Grande Cascade unit, which is a vesicle-free, phenocryst-rich, trachytic flow in the Monts Dore massif, France. Field work was carried out to define internal structures, and oriented samples were collected for chemical, petrological, and anisotropy of magnetic susceptibility analyses, allowing us to estimate emplacement temperature and viscosity.

These data allow us to define a new silicic lava flow subtype that is low in temperature (800–900 °C), high in silica content (up to 66.8 wt%), high in viscosity (10^9–10^{11} Pa s), rich in phenocrysts (~35%), and lacks vesicles. Brittle deformation of the lava occurs upon extrusion, generating a cataclasite basal layer and thin (3-m-thick) shear zone that accommodates all of the stress, allowing most of the flow's volume to slide over its base as a 40-m-thick plug in which there is no deformation. Blocks are rare, of a single size (10 ± 1 cm), and result from localized breakup of the basal shear zone.

Emplacement dynamics are different from those of glassy, pumiceous lava flows. They are closer to glacier dynamics, where most of the volume slides over a thin basal shear zone and till is generated there by abrasion and milling of the underlying layer. For the Grande Cascade lava flow, abrasion means that the flow lacks its classical blocky crust and instead the flow base is marked by a layer rich in fine-grained material. The structures and emplacement dynamics of this crystal-rich flow are consistent with ideal, gravity-driven shear flow. We thus argue for a global reassessment of silicic-rich lava emplacement based on crystal content and using a multidisciplinary approach focused on well-exposed examples in the rock record.

INTRODUCTION

Non-explosive silicic eruptions represent a ubiquitous style of volcanism that occurs in every geodynamic setting. Effusion of silicic lava, i.e., $SiO_2 > 63$ wt% (Le Maitre et al., 2002), is characteristic of subduction zones and continental rift zones (Wilson, 1989) but is also observed on oceanic islands (e.g., Self and Gunn, 1976; Nielson and Sibbett, 1996; Wiesmaier et al., 2013) and at some mid-oceanic ridges (Wanless et al., 2010). Extrusive activity results in the emplacement of voluminous domes, as well as flow lobes and silicic lava flows. Here we distinguish between flow and lobe using aspect ratio (i.e., unit length divided by width), where flows have aspect ratios of >3–5 (Walker, 1973; Wadge and Lopes, 1991). In addition, silicic lava flows typically have lengths greater than 1.5 km (e.g., De Silva et al., 1994; Harris et al., 2003; Lara et al., 2004; Tuffen et al., 2013; Auer et al., 2018; Bullock et al., 2018). Our focus here is on the emplacement dynamics and associated structures of silicic lava flows.

Previous work has found an array of structural and textural characteristics in silicic lava flows (e.g., Fink, 1983; Manley and Fink, 1987; Anderson and Fink, 1992; Dadd, 1992; Smith and Houston, 1994; Smith, 1996; Castro and Cashman, 1999; Castro et al., 2002; Magnall et al., 2017). Manley and Fink (1987) defined five textural facies that have since been found at most rhyolitic lava flows: coarsely vesicular pumice, finely vesicular pumice, obsidian, crystalline rhyolite, and breccia. Common structures include "crease structures" (Anderson and Fink, 1992), folds (Smith and Houston, 1994), and flow banding (Tuffen et al., 2003; Gonnermann and Manga, 2005). However, these studies have focused on glassy lava flows mostly composed of obsidian and microlitic lava.

Studies of phenocryst-rich silicic lava flows include work on the crystal-rich andesitic lava flows of the Michoacán-Guanajuato monogenetic field (Chevrel et al., 2016a, 2016b; Reyes-Guzmán et al., 2021; Ramírez-Uribe et al., 2021) and Popocatepetl (Ramírez-Uribe et al., 2022). Apparent viscosities for such flows are up to 10^8–10^{12} Pa s, which implies that these voluminous (up to 10^9 m^3) lava flow fields are emplaced very slowly over periods of months to years. Studies of crystal-rich, dacitic lava flows active at Santiaguito, Guatemala, have shown them to be slow moving (a few meters per day) but long-lived (active for several years) and capable of extending several kilometers (e.g., Rose, 1987; Anderson et al., 1995; Harris et al., 2003; Escobar-Wolf et al., 2010). Although active, Santiaguito's lava flows are not exposed, and comparison with a crystal-rich, trachytic flow exposed at the Puy de Cliergue in the Monts Dore massif of Central France by Latutrie et al. (2017) revealed quite different structures and associated flow dynamics. For example, the lava flow emplaced in January 2000 at Santiaguito had a "caterpillar-track–type advance" similar to *'a'ā* flows (Harris et al., 2002). But the Puy de Cliergue trachytic flow "slid" over a basal breccia and shear zone in a "glacier-like" motion (Latutrie et al., 2017). Flow surfaces at Santiaguito, as well as at the 1980–1986 Mount St. Helens dome and Unzen (Anderson et al., 1998), were characterized by a blocky surface (Rhodes et al., 2018). But the Puy de Cliergue unit was characterized by

†Corresponding author: andrew.harris@uca.fr.

 https://doi.org/10.1130/B36415.1; 14 figures; 3 tables; 1 supplemental file.

fine-grained matrix containing matrix-supported clasts, where rounding of clasts and matrix support was proposed to be consistent with clast abrasion, grinding, and crushing (Latutrie et al., 2017). Siebe et al. (2014) also observed that deposits exposed in lateral levees in thick, crystal-rich andesitic flows in Mexico resembled glacial moraines.

Hence, we appear to have two types of silicic lava flows (crystal-poor and crystal-rich), one well described, analyzed, and understood, and the other less so. To better define this second flow type, we studied a second crystal-rich, trachytic flow in the Monts Dore massif that is well exposed over a 300 m cross-flow distance. We defined internal structures, collected oriented samples for chemical, petrologic, textural, and anisotropy of magnetic susceptibility (AMS) analyses, and defined the grain-size distribution and particle morphology of the basal breccia. These data allow full definition of this new crystal-rich, silicic lava flow type and allow us to make inferences about the associated emplacement dynamics. We show that most stress is accommodated by brecciation, abrasion, and shearing of a thin basal layer, and most of the flow's volume slides over this basal layer as a plug with no deformation.

A Note on Terminology

We distinguish between crystal-rich and crystal-poor silicic lava flows. Crystal-rich is used for flows with phenocryst contents of >20–30% (cf. Latutrie et al., 2017) and up to 50–60% (Chevrel et al., 2016b; Ramírez-Uribe et al., 2021, 2022). Crystal-poor is used for obsidian-bearing flows at classic case-types of locations such as Little Glass Mountain (Fink, 1983) and Obsidian Dome (Castro et al., 2002) in the Western USA, or Rocche Rosse and Pietre Cotte (Bullock et al., 2018) in the Aeolian Islands of Italy. Our results, interpretations, and conclusions thus apply to crystal-rich, silicic lava flows and not to crystal-rich domes and lobes, or to crystal-poor cases.

Geological Setting

Located in the NW of the French Massif Central (Fig. 1), the Monts Dore volcanic complex comprises two stratovolcanoes: Guéry, active at 3.09–1.46 Ma (Nomade et al., 2014), and Sancy, active at 1.10–0.23 Ma (Nomade et al., 2012). The Grande Cascade unit was emplaced at 0.38 ± 0.02 Ma (Cantagrel and Baubron, 1983). The unit belongs to the "massif adventif" of Sancy, a group of ~10 N–S-aligned trachytic domes and flows that are petrographically similar to but younger than the rest of the Sancy massif and represent its last activity (Glangeaud, 1919).

The Grande Cascade ("the Tall Waterfall") is a ~35-m-high waterfall that drops from the Durbise plateau into Haute-Dordogne valley on its east side (Fig. 1). The Haute-Dordogne is a glacial valley carved during the last three glacial episodes (Etlicher and De Goër De Hervé, 1988). The waterfall is easily walked to from the Mont-Dore village (https://www.sancy.com/circuits/circuits-randonnee/randonnee-grande-cascade/). It has long been an iconic tourist site, which is evidenced by numerous ancient postcards of the site digitized by the Archives Départementales du Puy de Dôme, e.g., Figure 2A (http://www.archivesdepartementales.puydedome.fr/). The Grande Cascade is listed in tourist and walking guides (e.g., Fédération française de la randonnée pédestre, 2018; Delabroy et al., 2019; Michelin, 2019) and featured in geology field guides (e.g., Graveline, 2002; Chamina, 2003; Richet, 2003). It is ranked number one among 400 waterfalls in the region (Kalmar and Chassain, 2012) and, since 2016, it has been listed in the National Inventory of the Geological Heritage (Inventaire National du Patrimoine Géologique). It is also within one of the 58 regional natural parks of France, the *parc naturel régional des Volcans d'Auvergne* (Fédération des Parcs, 2021).

The cliff behind the waterfall laterally exposes a massive, ~40-m-thick trachyte lava flow ~300 m wide, which offers continuous exposure of all components of a crystal-rich, silicic lava flow system (Fig. 2). The unit, mapped by Scrope (1827) and Lecoq and Bouillet (1830), overlies a succession of older basaltic lava flows and pyroclastic deposits (Fig. 3).

METHODS

Different facies were defined by four criteria: geometry, lithology, structures, and movement patterns (Cas and Wright, 1987).

Flow Geometry and Structures

To infer the length, width, slope, and area of the Grande Cascade flow, we used the 1:50,000 geological map (Brousse and Tempier, 1981; Brousse et al., 1989), 1:25,000 topographic map (Institut national de l'information géographique et forestière, 2016), 10-m resolution Digital Elevation Model (CRAIG-TopoGEODIS, 2009), and orthophotographs with a 0.25-m resolution (CRAIG-SINTEGRA, 2013). Field measurements allowed us to define variations in the thickness and geometry of the unit and its component layers, and we mapped and measured all flow structures, such as shear and foliation planes and striations.

Textural Analysis

Anisotropy of Magnetic Susceptibility

AMS determines the petrofabric of igneous rocks and reflects the spatial arrangement and relative abundance of para- and ferromagnetic minerals, which depend on emplacement mechanisms and deformation history (Khan, 1962; Hrouda, 1982; Cañón-Tapia, 2004). Magnetic susceptibility (k) defines the linear relationship between an external magnetic field (H) applied to a material and the induced magnetization of the material (M):

$$M = kH \tag{1}$$

M and H being in A m^{-1}, and k being dimensionless. If the material is magnetically anisotropic, M is not parallel to H, and the relationship becomes:

$$M_i = k_{ij}H_j (i, j = 1,\ 2,\ 3) \tag{2}$$

in which k_{ij} is the second-order susceptibility tensor. The three values $k_{11} \geq k_{22} \geq k_{33}$, usually denoted as $k_1 \geq k_2 \geq k_3$ (or $k_{max} \geq k_{int} \geq k_{min}$), are the principal susceptibilities (Tarling and Hrouda, 1993). AMS is geometrically represented by an ellipsoid with axes parallel to the principal directions and semi-axis lengths equal to the principal susceptibilities. The k_3 direction defines the pole of the magnetic foliation plane, and the k_1 and k_2 directions lie on it, with k_1 giving the direction of magnetic lineation. Magnitudes of k_1, k_2, and k_3 are used to derive several descriptive parameters (as listed in table 1.1 of Tarling and Hrouda, 1993). Of these, we use k_1, k_2, and k_3 to obtain mean magnetic susceptibility (k_m):

$$k_m = \frac{k_1 + k_2 + k_3}{3} \tag{3}$$

corrected anisotropy degree (P_j),

$$P_J = \exp\sqrt{2\left[\begin{matrix}\left(\eta_1 - \eta_m\right)^2 + \left(\eta_2 - \eta_m\right)^2 \\ + \left(\eta_3 - \eta_m\right)^2\end{matrix}\right]} \tag{4}$$

shape parameter T (where i = 1, 2, or 3),

$$T = \left(2\eta_2 - \eta_1 - \eta_3\right)/\left(\eta_1 - \eta_3\right) \tag{5}$$

where $\eta_i = \ln\ k_i$, and $\eta_m = (\eta_1 + \eta_2 + \eta_3)/3$. Shape parameter T assesses the ellipticity of the AMS ellipsoid ($T > 0$ for oblate susceptibility ellipsoids; $T < 0$ for prolate).

We collected oriented cores and oriented hand samples at seven sites (GC1 to GC7) (see

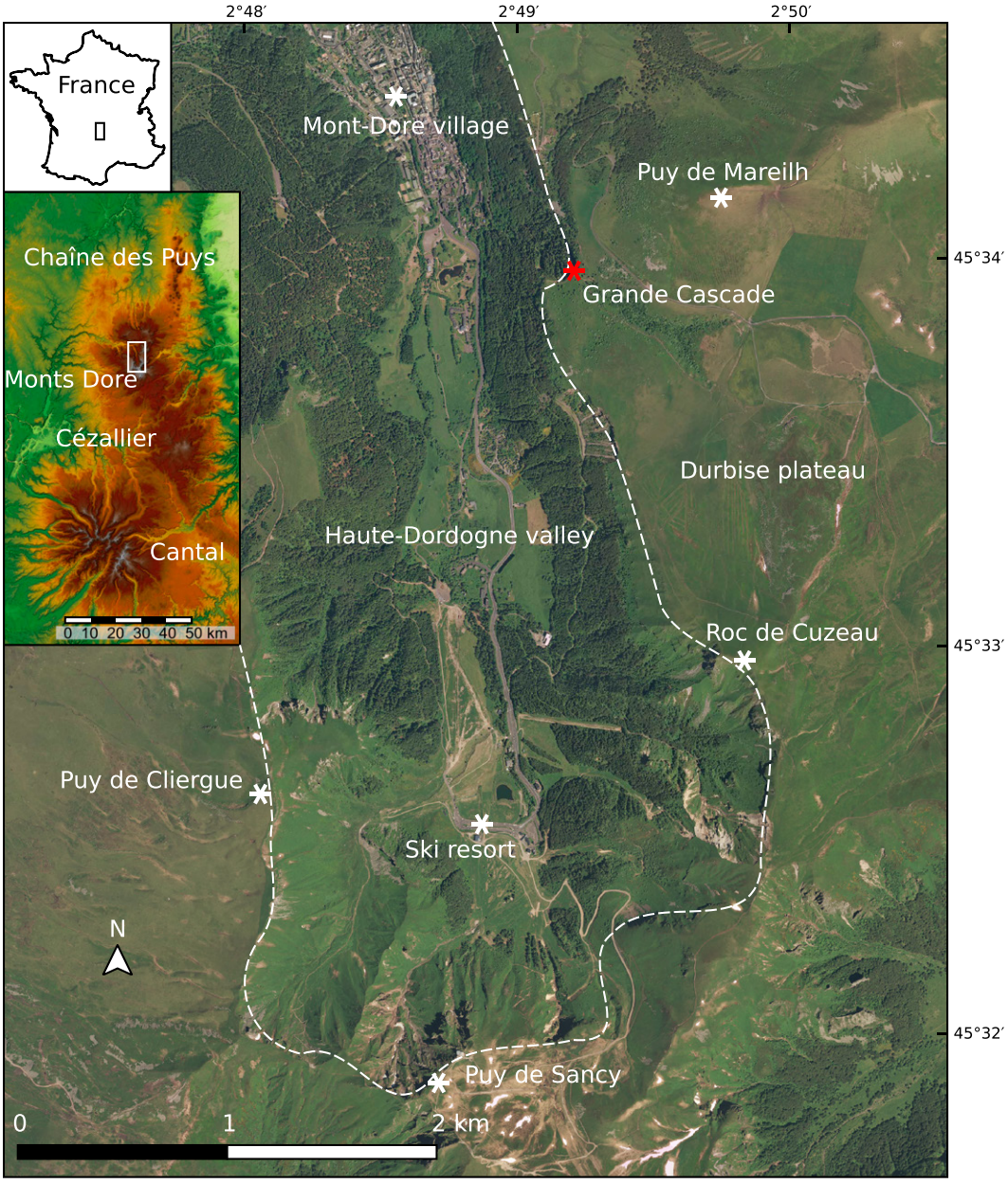

Figure 1. Orthophotograph of the Haute-Dordogne valley shows the location of the Grande Cascade and other sites mentioned in the text. Inset shows the topography of the four volcanic massifs of northwest Massif Central.

Table S1 in the Supplemental Material[1]). Some sites were divided into sub-sites to check for spatial coherency over 1–2 m. All measurements were performed at the Alpine Laboratory of Paleomagnetism in Peveragno, Italy. Bulk magnetic susceptibility and anisotropy were measured using an AGICO Kappabridge KLY-3 for 280 specimens. AMS data were then cleaned to remove outliers (Borradaile, 2003).

[1]Supplemental Material. Full list of samples with geographic coordinates and orientations. Please visit https://doi.org/10.1130/GSAB.S.21075583 to access the supplemental material, and contact editing@geosociety.org with any questions.

Breccia Particle-Size Distribution, Componentry, and Particle Morphology

We analyzed particle-size distribution (PSD) of the basal breccia along with the componentry and morphology of breccia particles. A ~4 kg sample of breccia was dried in an oven for 24 h at 70 °C, then sieved at a ϕ/2 interval. We calculated the corresponding grain-size parameters with Folk and Ward (1957) equations and the fractal dimension following Turcotte (1986). Assuming a spherical shape, PSD was converted from a weight to a number distribution using the particle density. The number (N) of particles larger than size L was then plotted in a log(N)-log(L) diagram on which data following a power law will plot as a straight-line segment, the slope of which defines fractal dimension D.

Componentry was determined by manually sorting particles under a stereo microscope. For each bin between 0ϕ (1000–1400 μm) and 4.5ϕ (44–63 μm), we analyzed a random selection of particles (a few hundred for the largest up to ~20,000 for the finest) with a Malvern Panalytical Morphologi G3. The G3 software outputs particle area (A_p), the area of its convex hull (A_{ch}), and corresponding perimeters P_p and P_{ch}, which were used to calculate the morphological parameters of Table 1.

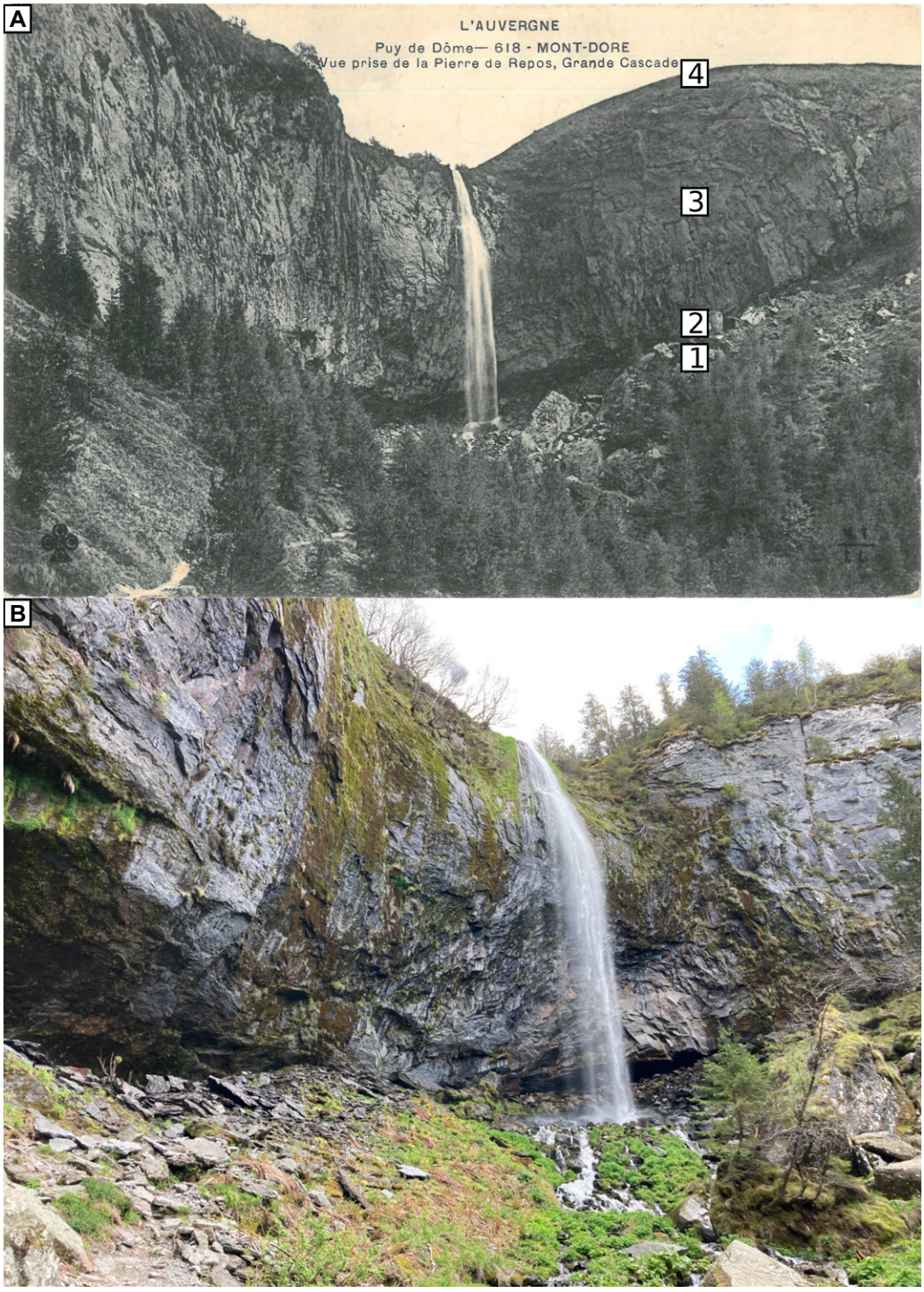

Figure 2. (A) Postcard of the Grande Cascade from around 1930 is shown. The waterfall is ~35 m high, and orientation of the cliff is N–S. Forest obscures this view today. Numbers of facies discussed in text: (1) basal breccia, (2) shear zone, (3) massive plug, and (4) surface. (B) Closer modern photograph looking northwest up to the Grande Cascade.

Chemical and Physical Properties of the Lava

Petrography, Chemistry, and Geothermometry

We performed petrographic and chemical analyses on the most representative samples of each facies. Bulk-rock major-element composition was determined via inductively coupled plasma–atomic emission spectroscopy (ICP-AES). Petrography was carried out on hand samples and two thin sections from the lava flow interior (the plug). Minimum phenocryst content was taken as the ratio between total crystal area and area of the scanned cut face of the sample and thin section (see Supplemental Material). Crystal aspect ratio was then determined as the ratio of the large and short axis of an equivalent ellipsoid, a value that approximates phenocryst volume fraction (Heilbronner and Barrett, 2014).

Gourgaud (1985) determined emplacement temperature of the Grande Cascade flow as

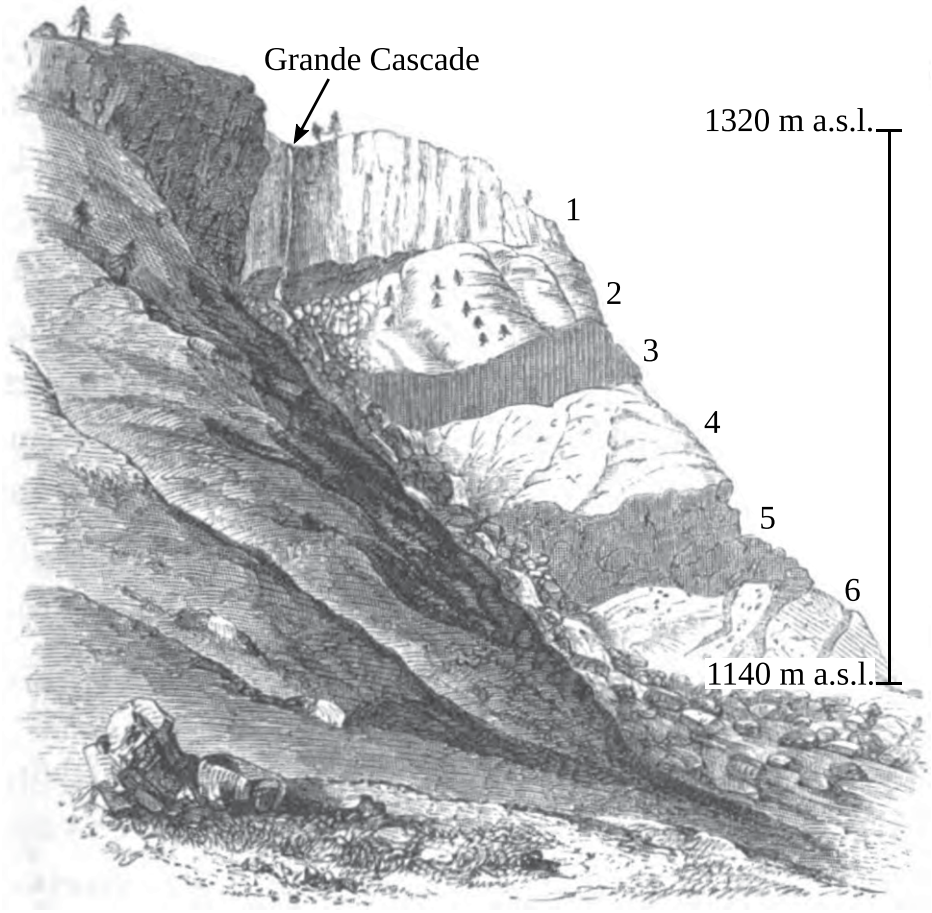

Figure 3. Geological sketch viewed toward the southeast shows the full Grande Cascade sequence (after Scrope, 1827, plate XI). The Grande Cascade trachytic flow is unit 1. Units 2, 4, and 6 are pyroclastic deposits, and units 3 and 5 are basaltic lava flows.

816–880 °C by applying magnetite-ilmenite (Powell and Powell, 1977) and plagioclase-liquid (Kudo and Weill, 1970; Drake and Weill, 1975) geothermometers. We reused Gourgaud's (1985) crystal and groundmass chemical-composition data with the plagioclase-liquid thermometer, the alkali feldspar-liquid thermometer, and the two-feldspar thermometer in Putirka (2008), along with the magnetite-ilmenite thermometer of Ghiorso and Evans (2008).

Viscosity and Density

Lava viscosity was estimated considering a two-phase mixture of melt (i.e., the matrix) and crystals (for methodology, see Chevrel et al., 2013, 2016b; Latutrie et al., 2017; Reyes-Guzmán et al., 2021). This method involves first estimating the liquid phase viscosity (η_{liq}) using the major element composition and emplacement temperature in the model of Giordano et al. (2008). Second, to account for the effect of crystals, we calculate the relative apparent viscosity (η_r) via the Krieger and Dougherty (1959) equation using the crystal volume fraction (see Supplemental Material for further details). The lava mixture (liquid + crystals) viscosity, η, is then calculated as $\eta_{liq} \times \eta_r$. Lava dense-rock equivalent (DRE) density was obtained from the ratio between sample mass and volume of the powdered sample obtained using a Micromeritics AccuPyc II 1340 gas displacement pycnometer (for method, see Thivet et al., 2020).

TABLE 1. KEY SHAPE PARAMETERS USED IN THIS STUDY

Shape parameter	Abbreviation	Formula	Sensitivity
Form Factor	FF	$4\pi A_p/P_p^2$	Form and roughness
Convexity	CVX	P_{ch}/P_p	Roughness (textural)
Solidity	SLD	A_p/A_{ch}	Roughness (morphological)

Note: See Liu et al. (2015) for a comprehensive summary of shape parameters.

Yield Strength, Strain Rate, and Velocity

Following Cigolini et al. (1984), we calculated the velocity gradient using:

$$v_x = \frac{\rho g \sin\alpha h^2}{\eta}\left(1 - \frac{z^2 + 2h_0(h-z)}{h^2}\right) \quad (6)$$

where h, h_0, ρ, α, and g are respectively flow height, plug height, lava bulk density, underlying slope, and acceleration due to gravity. Equation (6) applies between the base of the flow, where $z = h$ and $v_x = 0$, and the base of the plug, where $z = h_0$ and $v_x = v_{max}$. On top of this shear zone, all velocities are the same, and the whole plug thickness moves at the maximum velocity. For a Bingham model, yield strength (τ_0) is classically given by:

$$\tau_0 = \rho g h_0 \sin\alpha \quad (7)$$

and strain rate (ε_z) by:

$$\varepsilon_z = dv_x/dz \quad (8)$$

dv_x/dz being the vertical velocity gradient.

RESULTS

We first consider flow geometry, geochemical, petrographic, and textural characteristics. Results are then presented facies by facies. Here, the four facies defined within the Grande Cascade flow based on macro-features are (1) basal breccia, (2) basal shear zone, (3) massive plug, and (4) the eroded surface (Fig. 2).

Flow Geometry

Although erosion has worked on the Grande Cascade lava flow for the last 0.38 Ma, the topography still allows us to infer its vent-proximal outline (Fig. 4A). A break in slope on the southwestern flank of Puy de Mareilh indicates the source of the flow (Fig. 4B), while two gullies define its lateral boundaries (Fig. 4A). The flow can be traced ~700 m to the SW before being cut by the cliff at the Grande Cascade. We thus have a minimum length, as the medial-distal section has been removed by glacial erosion. However, other crystal-rich, trachytic lava flows in the vicinity are up to 2.5 km long (Latutrie et al., 2017). To the south, the contact is lost under a more recent (0.23 ± 0.2 Ma) trachyandesite flow from Roc de Cuzeau (Fig. 1). The surface slope is ~20° and is continuous up

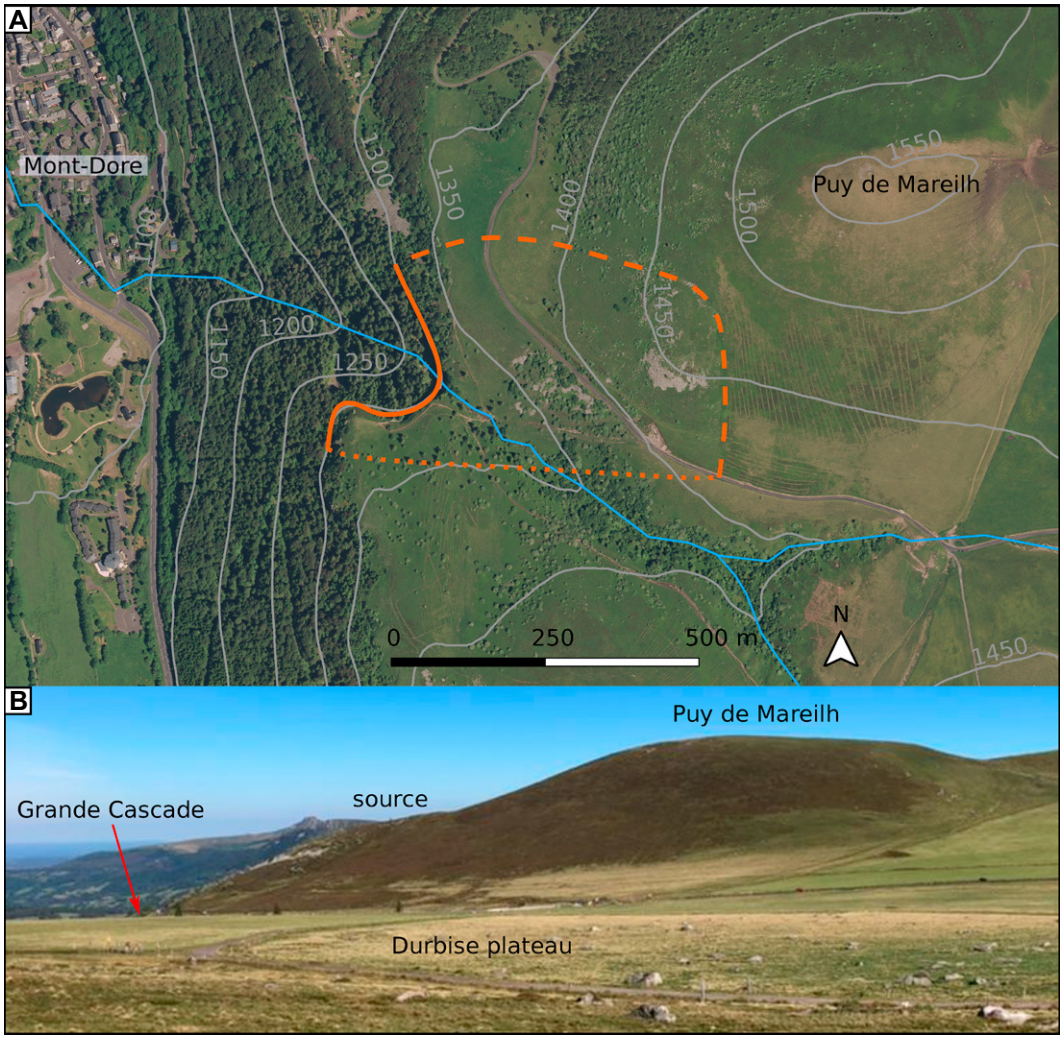

Figure 4. (A) Orthophotograph shows the Grande Cascade lava flow (orange) extending from the southwestern flank of the Puy de Mareilh dome. The solid line is the cliff where the flow is exposed. The dashed line represents the flow's limits inferred from topography, while the dotted line is where the contact is lost under a more recent lava flow. The blue line is the eponymous stream that feeds the Grande Cascade. All names given are as on ING (Institute Geographique National) map sheet 2432 ET (Massif du Sancy) on which the stream has no name but has its confluence at the Creux des Boeufs (Hollow of the Oxen). (B) Photograph taken from the Durbise plateau to the south shows the Puy de Mareilh dome and the bulge marking the source of the Grande Cascade flow on its southwestern flank.

to the break in slope at the base of the Puy de Mareilh (Fig. 4).

The Basal Breccia

A breccia crops out discontinuously the flow base. Most of the breccia layer is covered by talus of angular slabs fallen from the plug above. Exposures are up to 3–5 m thick, but in no place is the entire thickness exposed. The breccia matrix is dominated by rare centimetric to decimetric clasts surrounded by a gray, powdery matrix (Fig. 5). We found pockets of fine-grained breccia in the shear zone between shear-band–defined zones of solid rock. In most locations, we found no blocks, and 97% of the particles are smaller than 3.2–4.8 cm (Fig. 6A). At the southern end of the exposure there are around 30 10-cm blocks, one of them 70 cm in diameter, which are matrix-supported. Some of these blocks have their long axes aligned with the orientation of the shear zone (Fig. 5).

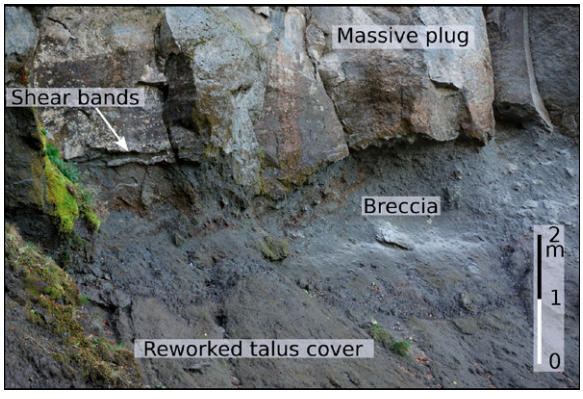

Figure 5. Breccia outcrop to the south of the Grande Cascade is shown. The sub-unit is at least 3 m thick, but its true thickness is greater, as the basal contact is covered by talus. Note the crude columnar jointing of the plug and shear bands between the plug and the breccia.

We had an insufficient number of blocks to complete statistical analyses of block-size distribution (cf. Anderson et al., 1998; Golombek et al., 2003; Bulmer et al., 2005). Of the 30 available, 29 had long-axis dimensions of 10 ± 1 cm. More than 6 wt% of the particles have diameters of <32 μm. The data are best fit by a Weibull distribution than a log-normal distribution, with residual square sums of 3.0 and 4.4, respectively (Fig. 6A). The PSD has a mean of 0ϕ, a standard deviation of 3.22ϕ (Table 2), and a fractal dimension of 3.36 ± 0.06 (Fig. 6B). In the 1ϕ fraction, particles have high values of convexity and solidity (medians of 0.915 and 0.942, respectively), meaning smooth, spherical particles (Fig. 7), with the ideal value being 1.0 for a circle. The values are similar for other grain

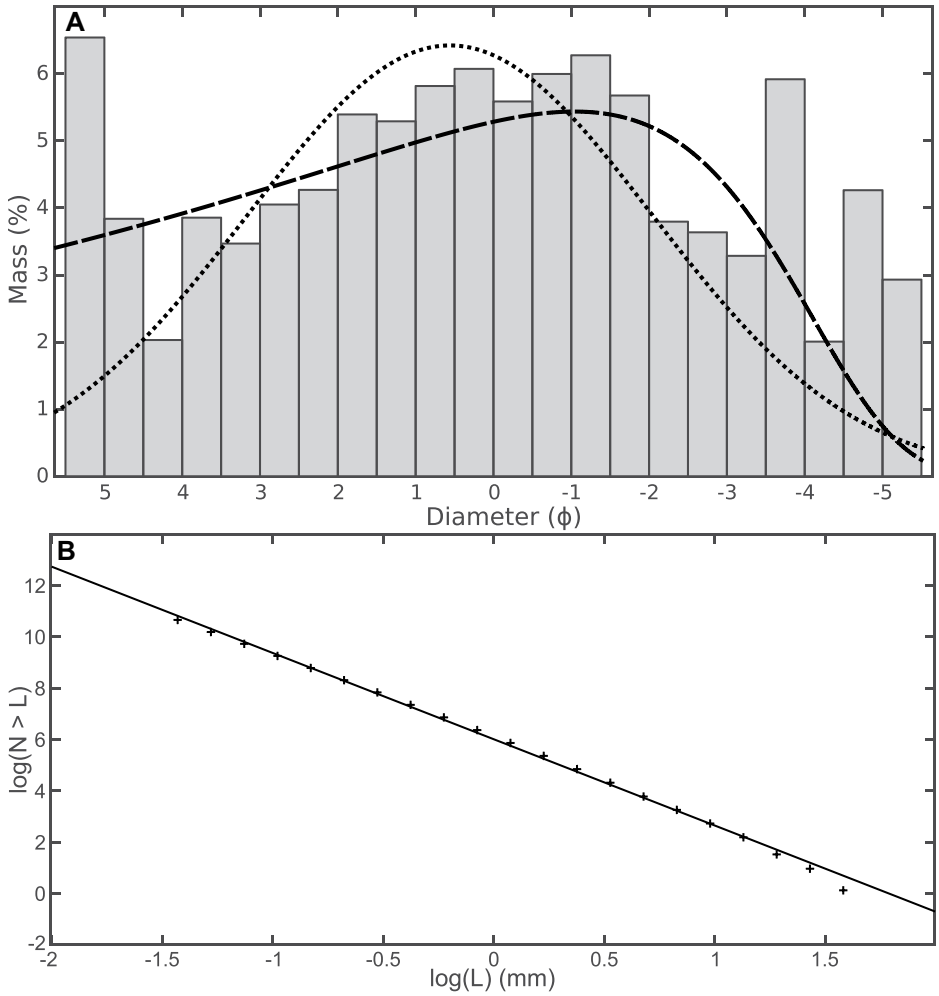

Figure 6. (A) Particle-size distribution of the breccia is plotted. Data fit with Weibull distribution (dashed line), and log-normal (dotted line) distributions are also shown. (B) Number, N, of particles larger than size L yield the fractal dimension of the particle-size distribution. Following Jones et al. (2016), we excluded the tail of the distribution (last data) from the fit.

sizes (median convexity of 0.899–0.919, median solidity of 0.926–0.950).

The breccia bulk composition is slightly less evolved than that of the lower part of the plug (Table 3). This difference can be explained by the assimilation of basic enclaves in the breccia. The breccia is also slightly denser than the plug base (2.76 g/cm^3 versus 2.70 g/cm^3). This is also compatible with the assimilation of denser basic enclaves in the breccia. Componentry analysis shows only three categories of particles in the breccia: 70% are lava, 29% are lava with crystals attached, and 1% are free crystals.

The Shear Zone

The shear zone crops out discontinuously at the base of the plug. Where the contact with the underlying breccia can be seen, the shear zone is typically ~3 m thick. Shear zone outcrops present sub-parallel shear planes (Figs. 8A and 8C), with frequency decreasing with height. At site GC1, there is one plane every ~7 cm at the base and one every ~14 cm at the top of the shear zone (Fig. 8B). At site GC3, frequency decreases upwards from one every ~12 cm to one every ~24 cm (Fig. 8D). At some outcrops, shear planes are more closely spaced (one every 1 cm, Fig. 8E), which indicates local variations in stress.

In places, shear planes coalesce to form shear bands filled with powdery lava with occasional rotated centimetric blocks (Figs. 8C and 8D), similar to a fault gouge (cf. Pallister et al., 2008). These bands are lighter toned than the surrounding lava due to the presence of ground sanidine crystals. To the SW, where the plug is only ~15 m thick, the shear zone is absent, and the plug lies directly on the basal breccia. At the center of the exposure where the plug is ~40 m thick, the shear zone is thickest.

The Plug

The plug is the main flow facies; it is 15–40 m thick and constitutes ~90% of the flow by thickness (Fig. 9A). Although massive, the plug presents few structures. Vertical fractures define crude (2–3-m-wide) columnar joints, which likely formed by thermal contraction of the lava upon cooling (cf. Mallet, 1875; Tomkeieff, 1940; Degraff and Aydin, 1987). The main structure is subvertical foliation, which defines 5–20-cm-thick slabs (Fig. 9B). These slabs provide an easy erosion surface. Slabs thus commonly detach from the cliff to contribute to a voluminous talus pile at the outcrop base (Fig. 2B). We found striated lava where the plug overlies the basal shear zone. Striations are ghost like, but parallel, and they extend ~2 m E–W, an indicator of flow direction.

Plug lava is vesicle-free and porphyritic, with white tabular plagioclase and sanidine megacrysts ($\leq$ 5 cm). This is typical of "sancyite," a local name for trachyte that contains large phenocrysts of sanidine and tridymite (Le Maitre et al., 2002). Millimetric phenocrysts include amphibole, clinopyroxene, and olivine, with occasional biotite. Olivine crystals are surrounded by pyroxene rims. Amphiboles commonly show a corona of oxide minerals, the result of a mixing process between two magmas that is a common phenomenon in the Monts-Dore massif (Gourgaud and Maury, 1984; Gourgaud, 1985). The trachyte matrix contains darker enclaves that are 2–30 cm in diameter. Enclaves have lobate shapes, glassy borders, and vesiculated cores that suggest a liquid state during incorporation in the host silicic magma. We interpret this as being associated with a more advanced stage of mixing

TABLE 2. MAIN PARAMETERS OF THE BRECCIA'S PARTICLE-SIZE DISTRIBUTION (PSD)

Parameter	Formula*	Value
Mean particle size	$\frac{\phi16+\phi50+\phi84}{3}$	0 ϕ
Standard deviation (sorting)	$\frac{\phi84-\phi16}{4}+\frac{\phi95-\phi5}{6.6}$	3.2 ϕ (very poorly sorted)
Fractal dimension	N.A.	3.36 ± 0.06

*ϕX is the ϕ value corresponding to the Xth percentile of the PSD.

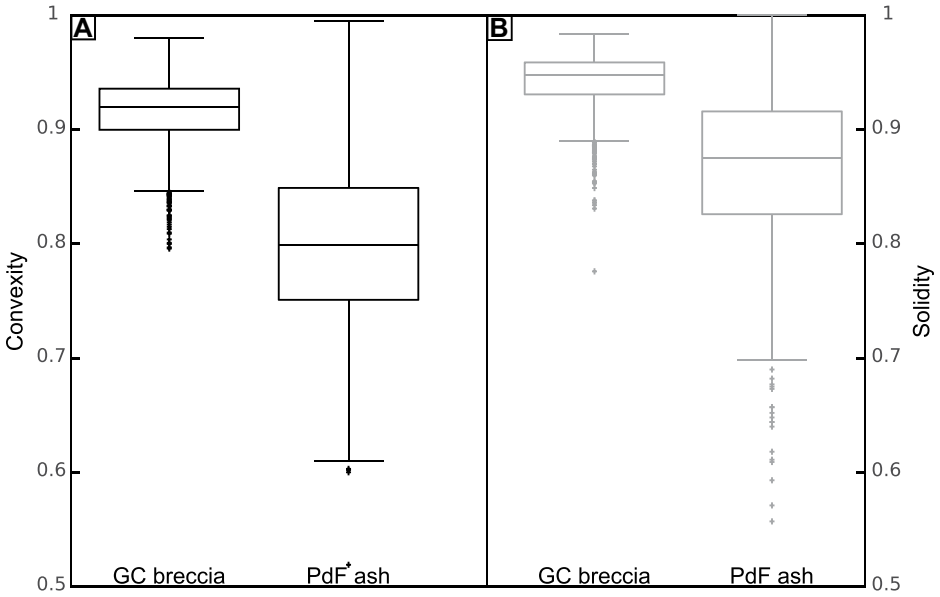

Figure 7. Diagrams show (A) convexity and (B) solidity of particles from the 1ϕ fraction of the Grande Cascade breccia (left, this study) and Piton de la Fournaise basaltic ash from the September 2016 eruption (right, from Thivet et al., 2020). In panel A, the 5–5.5ϕ bin includes all material finer than 5.5ϕ.

between two magmas. Plug lava is trachyte, and its silica content is ∼63 wt% (Table 3). The mean phenocryst content is ∼35 vol%, and its DRE density is 2.70 g/cm^3.

The Surface

The flow surface is covered by vegetation, and all surface breccia has been stripped away. Where exposure is available, it exposes the top of the plug zone. The Monts Dore massif was covered by ice during the last three glaciations: Mindel (ca. 480–420 ka), Riss (ca. 380–130 ka), and Würm (ca. 100–10 ka), in the Alpine nomenclature (Jung, 1946). The Haute-Dordogne valley was filled with 200–300-m-thick ice down to 8 km downstream of the Grande Cascade (Veyret, 1978). Considering the 0.38 Ma age of the Grande Cascade unit, it has endured the last two glacial episodes. Thus, any brecciated surface layer has been eroded. We found two outcrops on the northern side of the unit (at sites GC6 and GC7) and one in the streambed at the center of the unit (site GC5). At all three locations, the lava has similar foliation: 5–20-cm-wide, sub-vertical bands (Fig. 10). At the center of the unit, AMS data give a foliation strike of 80°, but to the north strike increases to 130° (Fig. 11). The lava is lighter toned, less dense (2.63 g/cm^3), and more silica rich (Table 3) than in the underlying shear zone. The plug zone thus represents a more evolved magma, tapped from the top of the reservoir. It was thus emitted first so as to be located at the top of the dome that then deformed SW to form the flow that we sample. Such a process is common in the Monts Dore massif (Gourgaud, 1985; Latutrie et al., 2017).

TABLE 3. MAJOR ELEMENT COMPOSITIONS OF THE GRANDE CASCADE LAVA

Facies	Surface	Plug	Breccia
Sample number	GC7-1	GC4-3	GCB
SiO_2	66.82	63.04	60.40
Al_2O_3	16.49	15.83	15.50
Fe_2O_3 tot	3.38	5.00	6.25
MgO	1.18	2.33	3.45
CaO	2.40	3.79	4.65
Na_2O	4.29	4.28	3.97
K_2O	4.30	3.97	3.59
TiO_2	0.76	1.22	1.56
MnO	0.08	0.13	0.14
P_2O_5	0.20	0.31	0.40
Ba	0.05	0.05	0.06
Sr	0.04	0.04	0.05

Note: Major elements are given in wt%. Sample coordinates are available in Table S1 (see text footnote 1).

Following Le Maitre et al. (2002), analyses were normalized to 100% on an H_2O- and CO_2-free basis.

Physical Properties of the Lava

Anisotropy of Magnetic Susceptibility

Mass susceptibility has a range of 546–12,587 × 10^{-9} m^3 Kg^{-1} with a mean of 6746 × 10^{-9} m^3 Kg^{-1}. Standard deviation are 50% due to low values of the surface facies (2241 ± 2068 × 10^{-9} m^3 Kg^{-1}), the high values in the plug (9805 ± 1727 × 10^{-9} m^3 Kg^{-1}), and highly dispersed values in the shear zone (Figs. 11C and 11D). The mean value of degree of anisotropy is low (1.038 ± 0.019) but shows significant variation (1.007–1.129). The magnetic fabric varies from prolate (−0.778) to oblate (0.965) depending on position in the flow. Facies show systematic variations that can be summarized as follows.

- Mean mass susceptibility varies from 10^{-2} –10^{-3} SI at the base of the flow to 10^{-3}–10^{-4} SI at the relatively silica-rich surface. This means that magnetite controls AMS in the more basic facies at the flow base, while paramagnetic minerals (likely biotite) control AMS in the more silicic facies toward the surface (cf. Tarling and Hrouda, 1993).
- The basal shear zone has a mean mass-susceptibility of 7385 ± 2690 × 10^{-9} m^3 Kg^{-1}. The AMS ellipsoid ranges from prolate to oblate, and there are two clusters of principal susceptibility axes (shear zone panels in Fig. 11). Thus, in fabric, two groups are observed in the shear zone:
  (1) An oblate magnetic fabric (at sites GC2, GC2-S1, GC2-S4, and GC4-2; see shear zone stereoplots in Fig. 11) with a horizontal to slightly imbricated magnetic foliation. The mean degree of anisotropy varies from 1.027 to 1.048. The principal susceptibility axes are clustered (Tables S1 and S2; see footnote 1). The magnetic lineation is horizontal with a WNW–ESE trend.
  (2) At sites GC2-S2, GC2-S3, GC3, and GC4-1 (Fig. 11), magnetic lineation trends WNW–ESE, but the magnetic foliation is steeper, with an inclination of 33–62°. The AMS ellipsoid is moderately oblate for GC2-S2 and GC2-S3 and strongly oblate at GC3 and GC4-1. The mean P_j is lower (1.017–1.027).
- At GC4 (Fig. 11A), we collected four samples from the bottom (GC4-1) to the top (GC4-5) of the shear zone. AMS ellipsoid changes progressively from oblate to neutral with height, and P_j decreases. Magnetic foliation dips east at an inclination of 28–53°, which is consistent with lower degrees of shear with height.
- Lowest mass-susceptibilities of all samples are at the surface. Magnetic foliation controls lineation, with slight (GC7, $T = 0.229$) to strong (GC5, $T = 0.720$; GC6, $T = 0.588$) oblate magnetic fabrics. Axes of k_1 and k_2 define a sub-vertical to vertical magnetic foliation, with an inclination of 65–87° (Fig. 11). Magnetic trends are consistent with a vertically oriented foliation.

Geothermometry

Temperature estimates range from 807 ± 30–970 ± 43 °C with a median of

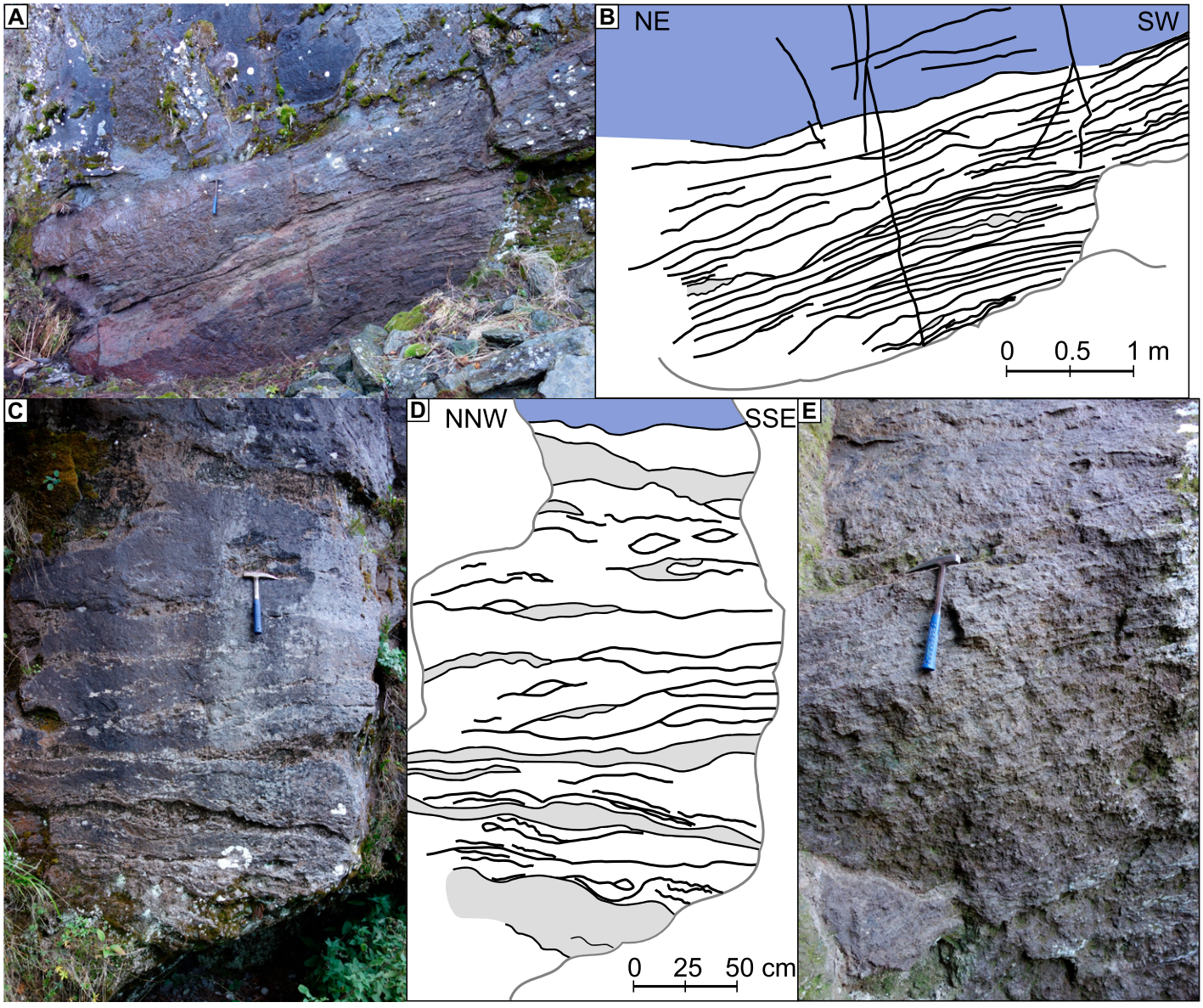

Figure 8. Photographs and sketches of basal shear zone outcrops are shown. (A) Outcrop at site GC3. (B) Corresponding sketch shows subparallel shear planes with a frequency decreasing with distance from the base. (C) Outcrop at site GC1. (D) Corresponding sketch shows 5–15-cm-thick shear bands (in gray) containing powdery lava. (E) Outcrop at site GC2 shows closely packed shear planes (about one every 1 cm). Hammer handle is 28 cm long.

~850 °C (see Supplemental Material). Our interval is consistent with Gourgaud's (1985) estimate, as well as with the data of Latutrie et al. (2017), who found emplacement temperatures of 873 ± 15–957 ± 15 °C for a similar trachytic flow on the western side of the Haute Dordogne valley (Fig. 1). The range is due to magma mixing, where many crystals show evidence of disequilibrium. Microlite crystallization may also have occurred in the conduit during the magma's slow ascent. Thus, temperatures should be considered maximum bounds for emplacement.

Viscosity

Viscosities calculated for the dry melt phase are 10^7–10^9 Pa s for a temperature range of 807–970 °C (see Supplemental Material). Adding a 35% volume fraction of crystals increases the viscosity to 6.9×10^{10} Pa s at 807 °C and to 2.2×10^8 Pa s for 970 °C. The lack of vesicles indicates that the magma was volatile poor when it arrived at the surface, which is consistent with silicic lava flows resulting from eruptions of highly degassed magma (Eichelberger et al., 1986; Taylor et al., 1983; Anderson and Fink, 1989; Anderson et al., 1995). Following Anderson et al. (1995), because the water content was likely low, we selected 0.1 wt% H_2O as an upper limit. This reduces the lava viscosity to 10^9 Pa s at 807 °C and 10^8 Pa s at 970 °C. We thus estimate viscosities of 10^8–10^{10} Pa s for the silicic fraction of the flow, which represents the bulk of the flow by volume (Supplemental Material).

Yield Strength, Velocity, and Strain Rate

Yield strength calculated with Equation 7 is 3.2×10^5 Pa. This compares with silicic flows at Santiaguito (1.3–6.7×10^5 Pa; Castruccio et al.,

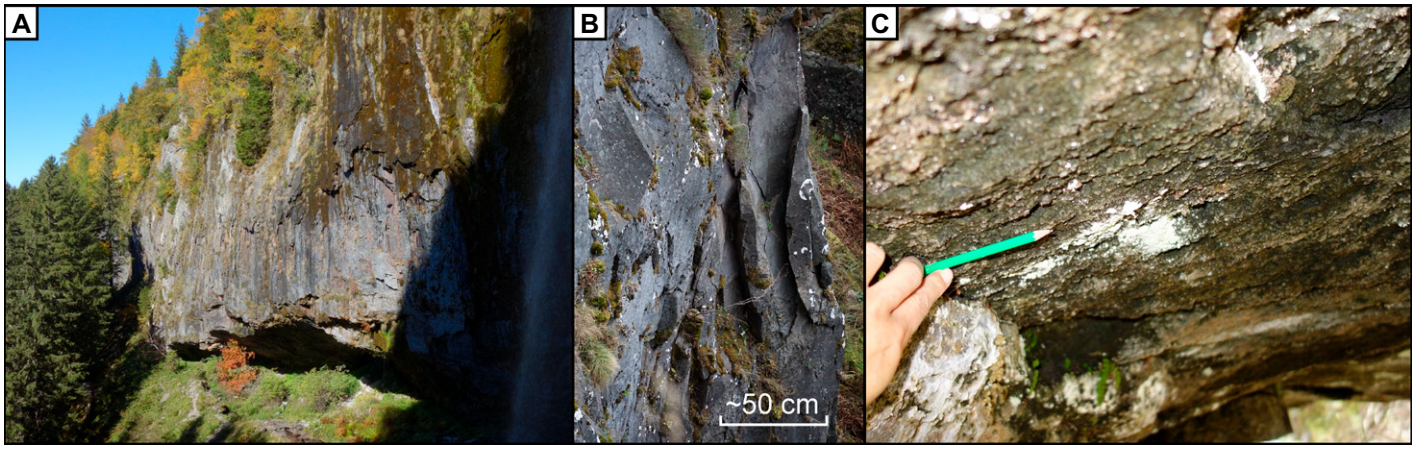

Figure 9. (A) Plug exposure seen from the waterfall shows the slabby form due to vertical foliation. Cliff face is ~40 m high. (B) Detail of the plug shows the sub-vertical foliation and slab formation. (C) Detail of the lave-etched striations under the plug; to show scale, a pen is parallel to the striations.

2013), Chao (8×10^5 Pa; De Silva et al., 1994), and Sinabung (2–11 $\times$ 10^5 Pa; Carr et al., 2018). It is also consistent with Blake's (1990) conclusion that "low lava domes and *coulees* develop if 10^4 Pa $\leq \tau_0 \leq 10^6$ Pa."

To account for the wide range of viscosities, we applied two velocity scenarios: (1) the highest possible viscosity for dry conditions at 800 °C, and (2) a most likely viscosity for a median temperature of 850 °C and 0.1 wt% H_2O. For the first scenario (Fig. 12), the flow has a maximum velocity of 1.45 $\times$ 10^{-5}m s^{-1} (~1 m day^{-1}). With the second scenario (Fig. 12), maximum velocity is 4.33 $\times$ 10^{-5}m s^{-1} (~4 m day^{-1}). These values are of the same order of magnitude as lava flows with similar silica contents. Manley (1992) estimated a mean velocity of 2–7 m day^{-1} for lavas of the Bruneau-Jarbidge system. At Santiaguito, velocities of the 2000–2002 flows were 2–13 m day^{-1} (Harris et al., 2004). At Cordón-Caulle, surface velocity estimates were 1.5–4 m day^{-1} (Tuffen et al., 2013; Magnall et al., 2017). At Sinabung, Nakada et al. (2019) measured velocities of 2–60 m day^{-1}, with the higher value corresponding to the initial phase, when slopes were steep (33°) and extrusion rates high.

Figure 10. Sub-vertical foliation crops out at the surface of the Grande Cascade unit. (A) Map view in the riverbed at site GC5 (north is up), and (B) overhead vertical view onto the hiking trail at site GC6 (east is up).

Figure 11. Anisotropy of magnetic susceptibility data for each site are grouped according to facies and sequenced according to position within the flow. The principal susceptibility axes are plotted on an equal-area, lower-hemisphere projection. Symbols: square—k1 direction; triangle—k2 direction; circle—k3 direction. Larger symbols with ellipses represent the site mean values and their 95% confidence limits (Jelinek, 1977). (A) Site locations in terms of cross-flow position along the base of the unit and across its surface. (B) Sketch of GC4 subsites. At GC4, sampling was completed up the sloping back wall of the overhang behind the waterfall, so samples were collected over a 5 m distance up flow and a 4 m distance vertically. The GC4 section thus crossed the shear zone from the basal breccia contact to the base of the plug. Hemispheres for the surface are for sites GC5, GC6, and GC7 of panel A. Hemispheres for the transition zone are for sites GC3, GC4, and GC-5 of panel B. Hemispheres for the shear zone are for sites GC1, GC4, GC3, and GC2 of panel A; (C) and (E) are graphs of *Xm* vs. *Pj* and *Pj* vs. *T*, respectively. Symbols: square—the shear zone; circle—a transition zone; rhomb—the surface. (D) Histogram of *Xm* for the different facies: black—the surface; dark gray—a transition zone; light gray line—the shear zone.

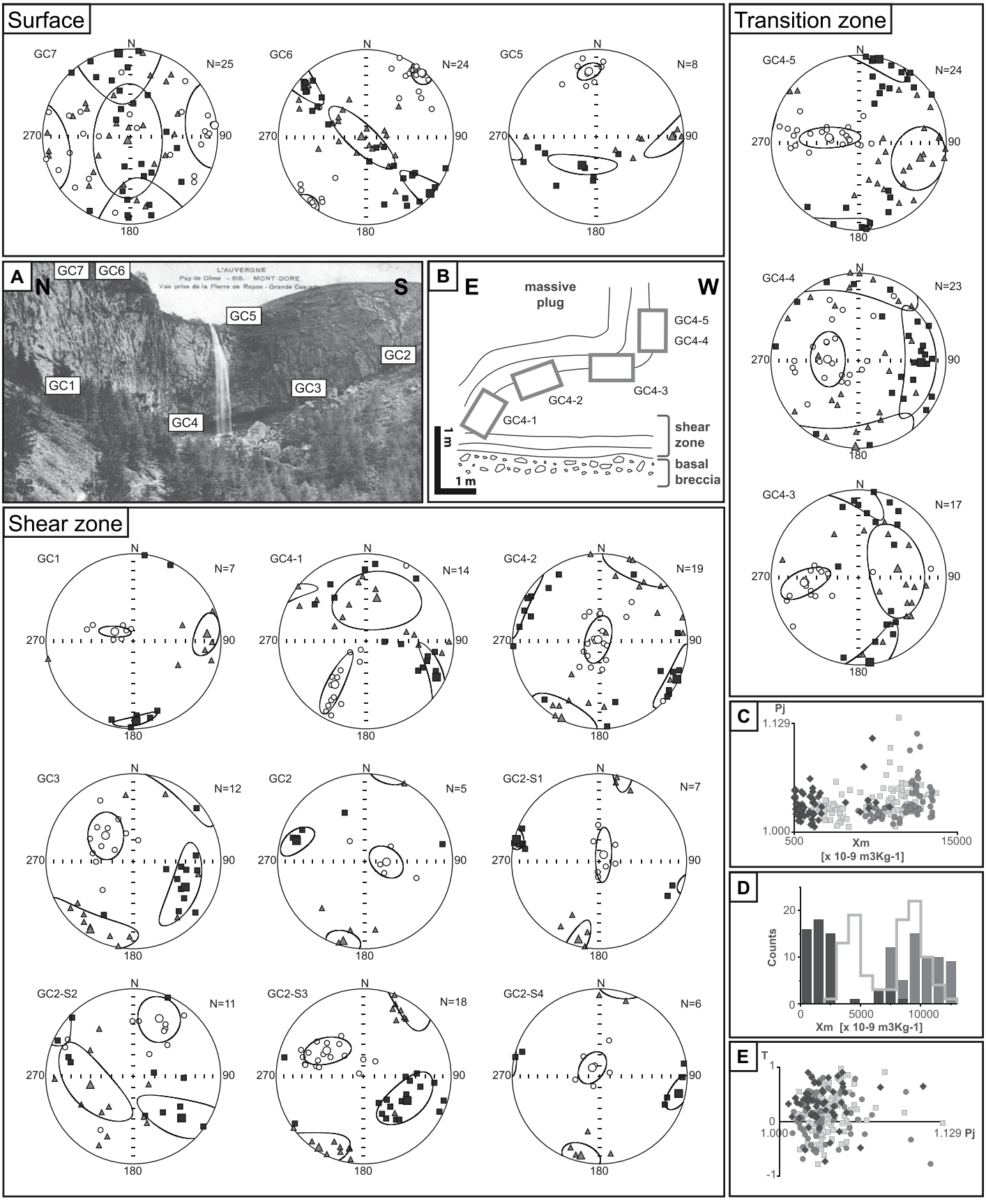
Surface
GC7
N=25
GC6
N=24
GC5
N=8
A
N
S
GC7
GC6
GC5
GC2
GC1
GC3
GC4
B
E
W
massive plug
GC4-5
GC4-4
GC4-3
GC4-2
GC4-1
shear zone
basal breccia
1 m
Transition zone
GC4-5
N=24
GC4-4
N=23
GC4-3
N=17
Shear zone
GC1
N=7
GC4-1
N=14
GC4-2
N=19
GC3
N=12
GC2
N=5
GC2-S1
N=7
GC2-S2
N=11
GC2-S3
N=18
GC2-S4
N=6
C
Pj
1.129
1.000
500
15000
Xm
[x 10-9 m3Kg-1]
D
Counts
20
10
0
5000
10000
Xm [x 10-9 m3Kg-1]
E
T
1
0
-1
1.000
1.129 Pj

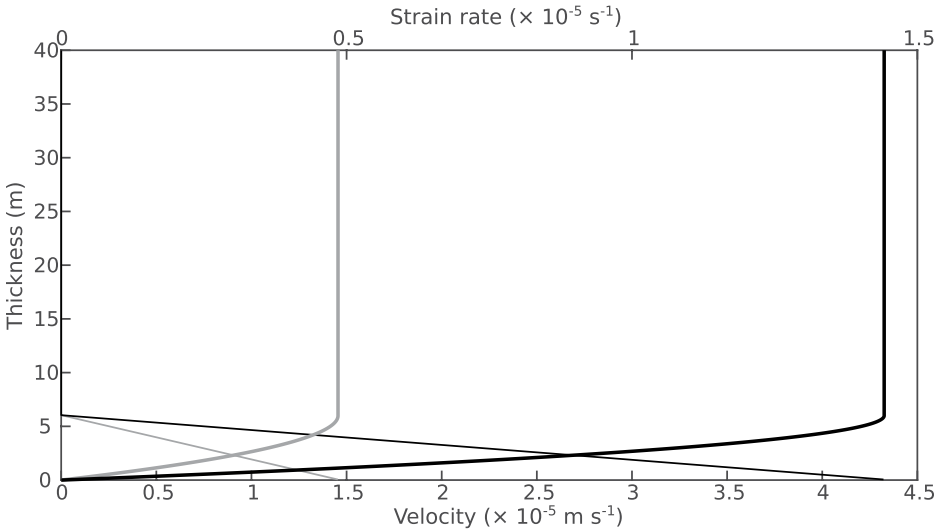

Figure 12. Velocity (thick lines) and strain rate (thin lines) profiles through the flow thickness are plotted. Velocity is zero at the base of the flow and increases up to a maximum value at the base of the plug. Strain rate is inversely proportional, and the plug moves at v_{max} with no deformation (riding along at the maximum velocity achieved at the top of the shear zone that carries the plug forward). Gray lines correspond to the scenario where the lava is at 800 °C and dry; black lines correspond to the scenario where the lava is at 850 °C and contains 0.1 wt% H_2O.

DISCUSSION

Origin of the Breccia

The breccia facies could be interpreted as a block-and-ash flow deposit. Rheomorphic ash-flow tuffs can also be hard to distinguish from silicic lava units (Henry and Wolff, 1992), and fragmentation of lava can occur during explosions at a flow base during passage over wet ground (e.g., Thorarinsson, 1953a; Greeley and Fagents, 2001; Hamilton et al., 2010). Here, we consider evidence for the breccia being generated by flow of the lava itself.

Fractal Dimension of the Particle-Size Distribution

PSD fractal dimension is linked to fragmentation energy and increases with the proportion of fine ash (Kueppers et al., 2006). For our basal breccia, the fractal dimension (3.36 ± 0.06) is similar to those of ignimbrite deposits, which range from 2.9 to 3.4 (table 2 in Kaminski and Jaupart, 1998). Kaminski and Jaupart (1998) obtained values of 4.2 that increased to 5.4 after a steel ball was added into the grinder. Jones et al. (2016) failed to produce $D > 2.45$ and concluded that high crystallinity prevents formation of fine ash because crystals are stripped of groundmass but are not broken. On the other hand, an increase in porosity favors an increase in D (Jones et al., 2016). Because the Grande Cascade trachyte has both high crystallinity and no porosity, it is difficult to determine their respective contributions to the fractal dimension. Milling is a kinetic process, and thus its duration influences D (Kaminski and Jaupart, 1998). Prolonged grinding of breccia beneath a slowly moving silicic lava flow could influence D. However, so too could explosive fragmentation (Kueppers et al., 2006). The fractal dimension alone is thus not sufficient to distinguish particles generated by magma decompression from particles generated by milling.

Morphology of the Particles

Our convexity (CVX: 0.899–0.919) and solidity (SLD: 0.926–0.950) shape-parameter values are too high for particles originating from magma fragmentation. Morphologi G3 data are scarce in the literature, but Thivet et al. (2020) analyzed basaltic ash from lava fountaining. They found rough particles, with median CVX and SLD of 0.798 and 0.874 for the 1ϕ fraction (Fig. 7). Buckland et al. (2018) used the Morphologi G3 to analyze ash produced by abrasion of pyroclasts placed in a mill for four minutes. They obtained SLD and CVX in the 0.94–0.98 range. These data show that the Grande Cascade basal breccia likely results from a milling process. The lack of lithic fragments in our basal breccia also provides evidence that component particles do not have an explosive origin. Instead, the identical geochemical and petrological affinity to the overlying lava and its enclaves points to the lava body as being the source. Given a ~40-m-thick lava body with an average density of 2650 kg/m^3, the base of the flow would be under a lithostatic pressure of ~1 MPa. We conclude that the basal breccia results from milling of the base of the main lava body.

Non-Blocky Basal Breccia: Mode of Formation

The brecciation process generating the basal crust at the Grande Cascade is different than the classical "rolling over" process typical of 'a'ā flows (Macdonald, 1953), where blocks from the upper crust fall and are overridden by the flow front (Harris et al., 2002). It also differs from a classic blocky crust that is typically associated with silicic lava flows (e.g., Finch, 1933; Anderson et al., 1998; Rhodes et al., 2018). Anderson et al. (1998) showed that block-size distribution reflects stress conditions at the vent, where high extrusion rates result in small primary blocks and low extrusion rates lead to larger blocks. Primary blocks then fracture through mechanical and thermal processes as they move down flow (Anderson et al., 1998; Bulmer et al., 2005). The result is an exponential form to the block-size distribution with a decrease in number with increasing diameter with distance (Golombek et al., 2003). The blocks we found were all the same size (10 ± 1 cm) and match the same dimension as the fracture spacing in the shear zone at the Grande Cascade (Fig. 8). Blocks are also aligned with the horizontal fracture sets in the basal shear-zone. Thus, we suggest that the rare blocks present in the basal breccia are due to isolated break-up of the shear zone. Subsequently, blocks are not broken further. Anderson et al. (1998) showed that blocks <12 cm do not accumulate on the flow surface because they slip toward the flow interior through void spaces between larger blocks. It seems that a reverse process occurs in the basal shear zone, where small blocks fall into the fine-grained matrix.

We thus see evidence of the basal shear zone breaking up into blocks in the same manner observed by Dadd (1992) and Smith (1996) at the base of a silicic lava flow. Dadd (1992) observed that the basal breccia could be found as pockets in the lowermost portion of the massive lava and concluded that this was consistent with mechanical fracturing in a zone of high shear stress. Smith (1996) also argued that in basal zones subject to high shear stress, brittle failure involves fracturing along horizontal shear planes as well as vertically. This fragments the basal shear zone into a blocky structure. In our case, we found these blocks to be rare and set in a fine-grained matrix more akin to a fault gouge.

Diamict Generation

The lithology of the basal breccia is that of a diamict, i.e., an unsorted to poorly sorted deposit with a wide range of grain sizes consisting of "floating" clasts in a fine-grained matrix

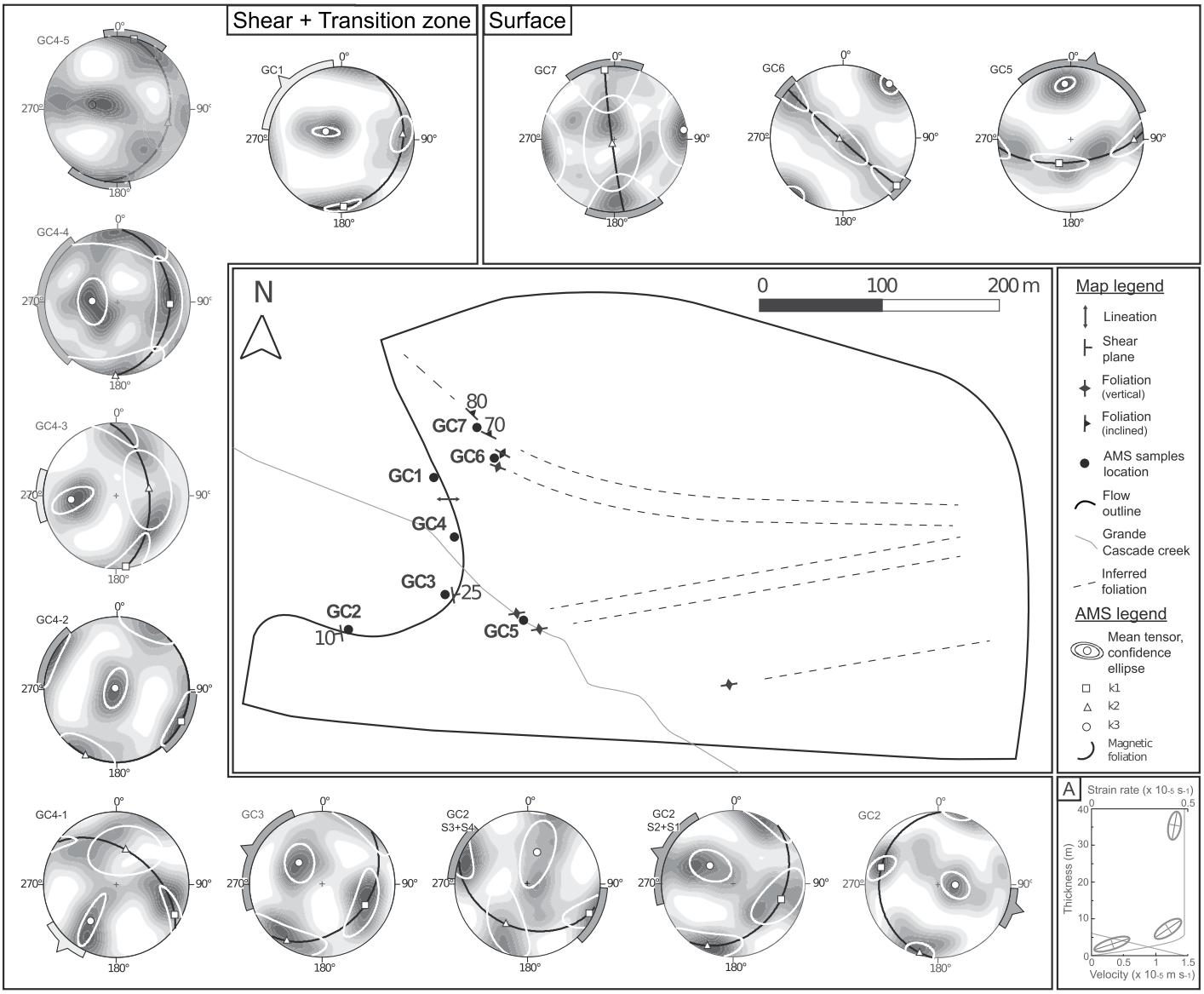

Figure 13. Structural map of the Grande Cascade flow, along with contour diagram of anisotropy of magnetic susceptibility (AMS) axes for each site. Directions of emplacement and relative error bars are marked at the perimeter of each hemispheric projection. Dark gray—direction defined using the magnetic lineation; light gray—direction defined through the foliation pole. In panel A, AMS ellipsoid projections along z–x planes (z—vertical, x—flow direction) are plotted on the calculated velocity and strain rate profiles and show alignment with these profiles.

(Menzies, 2009). Diamicts are found in a range of settings from glacial to sedimentary, and we found them at the sample site at the southern end of the exposure (Fig. 5). If lithified, such a deposit is called a diamictite (Flint et al., 1960), and this is the case toward the center of the exposure. Thus, the basal facies is an example of a diamict in a volcanic setting.

Magnetic Fabric: Flow-Dynamics, Emplacement Directions, and Paleosurface

AMS fabric reflects crystal orientation developed during molten state (Hargraves et al., 1991; Rochette et al., 1992; Akkoyun et al., 2013). It is thus widely used as a proxy to infer flow dynamics (e.g., Tarling and Hrouda, 1993; Cañón-Tapia, 2004; Loock et al., 2008). Magnetic lineation generally develops parallel to flow direction, so that k_1 coincides with flow and k_3 is perpendicular. This model is complicated by primary and secondary sources (Bascou et al., 2005), so that the original fabric can show varying degrees of overprinting (Schulmann and Ježek, 2012). For imbricated fabrics, use of magnetic foliation is more accurate (Hillhouse and Wells, 1991; Gurioli et al., 2007; Boiron et al., 2013). Here, depending on the situation, we used magnetic lineation or magnetic foliation to define emplacement direction and local variations in flow direction, and magnetic foliation was well defined in all parts of the Grande Cascade lava flow (Fig. 13).

Low values of mass susceptibility at the surface are associated with silica enrichment and Fe_2O_{3tot} depletion (Table 3). Inferred flow directions (Fig. 13) reveal movement toward the southwest and northwest. The sub-vertical magnetic foliation and oblate shape of the AMS is inherited from the conduit (cf. Závada et al., 2009), where foliation became aligned with shear around a vertically ascending plug.

At the flow base, higher χ_m relates to lower silica content and higher Fe_2O_{3tot}. Westward to northwestward emplacement directions are the same as striation directions at the plug base (Fig. 9C). Positive, progressive imbrication in the basal shear zone suggests that the maximum velocity occurs above this zone (cf. Caballero-Miranda et al., 2016). A decrease in velocity and increase in strain with depth across the basal shear zone is also reflected in the orientations of AMS ellipsoid projections (Fig. 11). This is consistent with the velocity and strain profiles expected at the base of the flow (Fig. 12).

Presence of magnetic lineation slightly transverse to the main flow direction is due to a component of lateral spreading that was probably induced by irregularities in the paleoslope (cf. Caballero-Miranda et al., 2016). The southwestern flow direction of sample GC4-1 likely relates to the presence of a small gully beneath the flow. The flow would have moved down the gulley, but it would have spilled over the sides, consistent with thinning to the NE and SW.

Internal and surface structures are not complex and involve only vertically orientated foliation. There are no complex structures such as folds, ramps, or extensional fabrics that would be consistent with flow moving over a break in slope (cf. Bullock et al., 2018). The lack of internal structure is also consistent with modeling by Gregg and Fink (2000) that generated a lack of structures for slopes of 10–30°. The paleoslope for the gulley down which the flow moved thus seems similar to those of today's surface: uniform and around 20°.

The relative increment of *Pj* and clustered principal magnetic susceptibility axes for samples in the shear zone can be associated with shearing and variable degrees of vertical shortening caused by the flow weight and hence thickness (Caballero-Miranda et al., 2016). Variation in *T* at the flow base can be related to interactions between the primary fabric and shear due to sliding of the plug over the shear zone (cf. Schulmann and Ježek, 2012). Sliding is consistent with our source model for the basal breccia, i.e., breakup of the shear zone under intense shear stress and grinding of blocks into a powder due to the weight and slow motion of the overlying plug.

Emplacement Model of the Grande Cascade Lava Flow

Our structural and textural data, as well as the sequence of facies, allow us to build an emplacement model with three steps (Fig. 14).

(1) Genesis of Cataclasite by Magma Milling and Generation of Vertical Foliation

The out-gassed, crystal-rich, and water-poor magma that fed the Grande Cascade flow had a high viscosity ($\geq 10^9$ Pa s) (Fig. 14A). During ascent, magma underwent shearing and milling against the conduit walls. This generated a cataclasite layer around the central plug and involved abrasion of the annular shear zone to form a matrix-dominated deposit. Extruding silicic lava bodies are known to produce fine-grained powders by grinding ascending, near-solid magma against conduit walls (cf. Bluth and Rose, 2004; Sahetapy-Engel et al., 2008). Cataclasite or fault gouge was observed in rhyolitic conduits by Tuffen and Dingwell (2005), and a similar phenomenon was documented during 2004–2008 dome extrusion at Mount St. Helens (Cashman et al., 2008; Kendrick et al., 2012; Pallister et al., 2008, 2013). Foliation also developed during ascent. Foliation is a common feature of silicic lava flows as, for example, in the dacitic flows of Crater Lake (Allen, 1936), Comb Peak rhyolite (Christiansen and Lipman, 1966), and Little Glass Mountain (Fink, 1983). Foliation generally develops in the conduit through shearing (de Lima et al., 2018). At the Grande Cascade, sub-vertical foliation inherited from magma ascent was imprinted on the lava (Fig. 14).

(2) Dome Extrusion

Extrusion built a low lava dome (senso Blake, 1990): the Puy de Mareilh (Fig. 1; Fig. 14B). Cataclasite formed the basal layer around the spreading dome and acted as lubricant to favor lateral deformation. The body began to spread downslope, following a gully to the west. Rare blocks were generated by brittle fracturing of the shear zone, but the basal breccia continued to be milled by the overlying plug. Shearing allowed

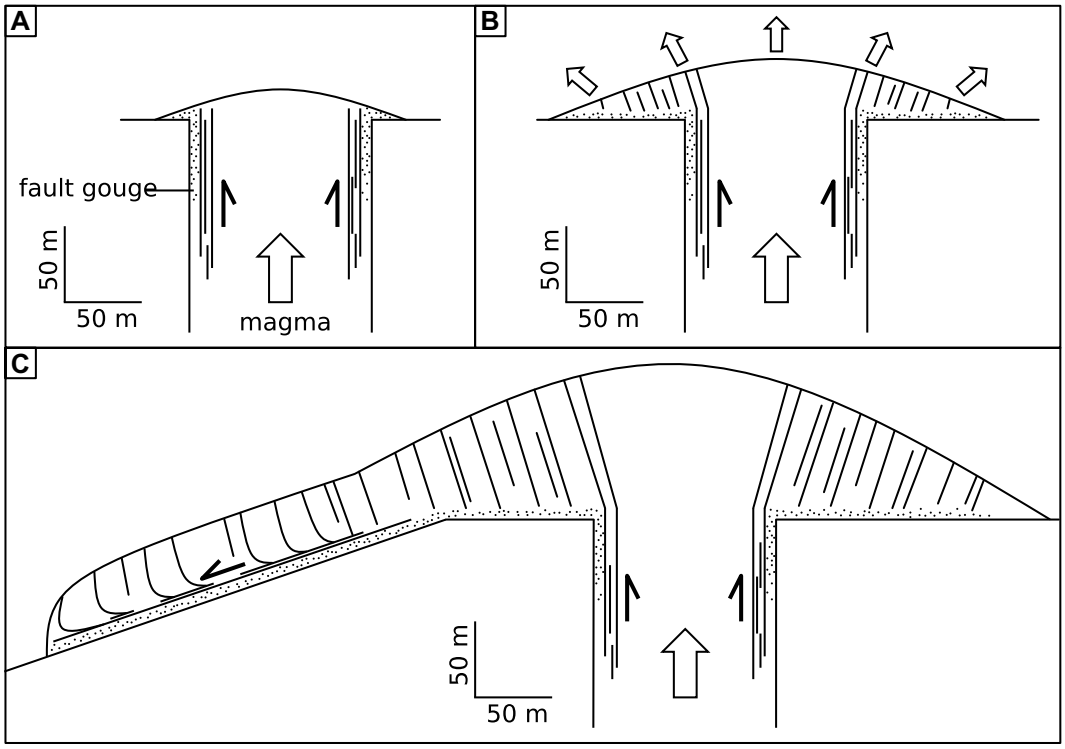

Figure 14. Three-step emplacement model of the Grande Cascade flow is shown. (A) Genesis of cataclasite by magma milling. (B) Dome extrusion and endogenous growth. (C) Formation and spreading of the flow downslope. This final panel serves as an idealized cross-section for such a flow case where the plug-dominated outcrop lacking deformation structures is consistent with simple shear in a gravity flow.

the solid plug to slide over the basal breccia, with the plug retaining its sub-vertical foliation inherited from the conduit.

(3) Formation of a Silicic Lava Flow

If a dome extends onto a slope, it begins to deform preferentially in the downhill direction (Blake, 1990) (Fig. 14C). Blake's (1990) Equation 37 allows us to estimate the critical radius, R, at which a dome will spread as a function of slope and yield strength. With $\theta = 20^{\circ}$ and $\tau_0 = 3.2 \times 10^5$ Pa, R is around 100 m. The length scale of the Grande Cascade unit, being greater than this threshold, means that spreading was possible, with deformation being accommodated by the basal shear zone and the plug sliding over this zone with no strain.

Fault gouge generated during ascent became the main component of the basal crust, and subvertical foliation inherited during ascent was retained in the plug. Minor, small, and uniformly sized blocks broke off from the basal shear zone to float in the fine-grained matrix of the breccia at the flow base as the plug slid downhill.

Spacing of flow-surface foliations (Fig. 10) is roughly the same as the fracture spacing in the basal shear zone ($\sim$10 cm). Foliations could thus have broken up to form a scattering of small (10 cm) blocks at the surface. However, the lack of shearing at the plug top (Fig. 12) would have meant that the surface would likely have been largely breccia-free and not composed of angular blocks of meter-scale dimension (cf. Finch, 1933; Anderson et al., 1998; Bulmer et al., 2005; Rhodes et al., 2018). Instead, the surface layer was likely composed of an easily erodible cataclasite similar to that remaining at the flow base, which formed around the ascending plug in the conduit (Fig. 12).

Analogies with Glacier-Flow Mechanics

Glacier motion is a combination of sliding of ice over its bed, plastic deformation, and/or deformation of the bed (Benn and Evans, 2010; Cuffey and Paterson, 2010). The first two processes are analogous to viscous flow of crystal-rich, silicic lava. Lava flow emplacement has long been compared to that of ice. On observing active lava at Vesuvius, Italy, Forbes (1846) mentioned that "the unexpected analogies presented by a torrent of fiery lava and the icy stream of a glacier." Forbes (1846) summarized the resemblance between lava and ice flow: their velocities are equally slow, similar morphological features, including ogives (Thorarinsson, 1953b), and their parts can be rigid, while the body is fluid.

Basal slip rates at glaciers varies from 0.008 m day^{-1} to 1.1 m day^{-1} (Cuffey and Paterson, 2010). Surface velocities are higher, but the basal-to-surface velocity ratio is as low as 0.03 (Cuffey and Paterson, 2010). Thus, as we found, there is a velocity gradient between the flow base and the overlying plug. In addition, velocities are similar, and the mass slips over its bedrock. Viscosities and yield strengths for glaciers are $\sim 10^9$–10^{13} Pa s and 5–6 $\times$ 10^4 Pa, respectively (Barnes, 1999; Fischer and Clarke, 1994). These are identical to those estimated for the Grande Cascade, so that similar flow regimes, structures and emplacement styles are to be expected. Indeed, Iezzi and Ventura (2000) found that strain patterns of the Porri lava flow on Salina (Italy) were similar to those described for surge-type glaciers by Lawson et al. (1994).

Formation of glacial till can be compared to the formation of the basal breccia at the Grande Cascade lava flow. In till, "grains evolve to finer sizes by abrasion and crushing," with a fractal dimension of 2.84–2.96 (Cuffey and Paterson, 2010). This matches our results, where lithification of the basal breccia at the Grande Cascade resulted in a diamict, a rock that is generally associated with glacial settings and tills (Menzies, 2009). Volcanology and glaciology are thus two disciplines that benefit from the understanding and modeling of emplacement dynamics; both involve high-viscosity bodies that slide and slip over a thin basal shear zone so as to mill its substrate into a fine, till-like powder.

Idealized Cross Section of a Crystal-Rich, Silicic Lava Flow: Implications for Flow Regime

Structures in outcrop at the Grande Cascade crystal-rich, silicic lava flow are less complex than those found in crystal-poor silicic lava flows (cf. Fink, 1983; Manley and Fink, 1987; Anderson and Fink, 1992; Dadd, 1992; Smith and Houston, 1994; Smith, 1996; Castro and Cashman, 1999; Magnall et al., 2017). For the crystal-rich case, the plug is monotonously dominated by vertical foliation inherited from shearing during magma ascent (Fig. 14), and the entire unit contains none of the structures commonly found in crystal-poor flows (e.g., Fink, 1983; Castro et al., 2002; Tuffen et al., 2013; Bullock et al., 2018).

We only found one exposure that is located 700 m from the source. However, this exposure cuts laterally across the entire flow width and reveals a simple cross-section involving a massive plug on a shear zone characterized by horizontal down-flow–oriented shear planes. The shear zone overlies a fine-grained deposit rather than the blocky crusts traditionally associated with silicic lava flows and domes (cf. Anderson et al., 1998). The unit also lacks both large- and small-scale folds and does not display the thrusts or ogives that are found in other crystal-rich cases (as in the cases of, for example, Iezzi and Ventura, 2000; Cioni and Funedda, 2005; De Silva et al., 1994; Chevrel et al., 2016b; Reyes-Guzmán et al., 2021; Ramírez-Uribe et al., 2022).

Shear structures that we do find (Fig. 8) are consistent with simple shear in a lava moving as an ideal shear flow (cf. Iezzi and Ventura, 2000). Stabilization of a plug-dominated velocity gradient (Fig. 12) with deformation in a direction predominantly away from the vent is also consistent with gravity-driven flow (cf. Fink, 1983; Smith and Houston, 1994; Castruccio et al., 2013). Lack of pure shear implies confined flow of solid, or near-solid, lava on a uniform slope (cf. Manley, 1996; Smith et al., 1993; Fink, 1983). The resulting idealized cross-section through this plug-dominated, gravity-driven flow is thus simple, as shown in Figure 14C. Observations and modeling have suggested that "simple shear strain increases and accumulates with distance from the source" (Iezzi and Ventura, 2000), and that near the source lateral extension, pure shear, and shear deformation dominate (Merle, 1998). Our case is vent-proximal and indicates that simple shear can dominate even at the source and that such crystal-rich lava flows can thus be gravity-driven shear flows throughout their length.

CONCLUSION

By analyzing structures, textures, and physical properties of the Grande Cascade trachytic flow, we built a three-step model for emplacement of high viscosity, crystal-rich, silicic lava flows emplaced on a uniform slope. Our model, and the resulting flow dynamics, structures, and facies, are very different from those of the classical emplacement model of crystal-poor silicic lava flows, where ductile deformation occurs at a large scale. In our case, the presence of massive lava lacking vesicles means that there are no pumiceous parts that can rise by diapirism (Fink, 1983; Fink and Manley, 1987; Manley and Fink, 1987). Our model instead applies to plug-dominated, gravity-driven, dense and crystal-rich flow. The Grande Cascade flow's high crystal content and low porosity led to emplacement of a highly viscous lava, which underwent a brittle behavior like that of glacier ice. Abrasion and grinding of the basal breccia results in the generation of diamict, which extends the provenance of this lithology to silicic lava flow settings.

Our study demonstrates the different methods that need to be applied to older lava flows that are partially eroded and/or covered by vegetation to decipher emplacement style and their

association with resultant internal structures and facies. Applying such an array of analysis techniques to older flows provides a means of better understanding emplacement mechanisms that are applicable to those of similar flow types. The emplacement dynamics and associated structures of this crystal-rich, silicic lava flow are very different from those of their crystal-poor counterparts, which argues for a global reassessment of silicic lava flow emplacement based on crystal content.

ACKNOWLEDGMENTS

We thank Stefano Mannini, Benjamin Van Wyk de Vries, and Alexander Wilson for joining us in the field and sharing their thoughts about the lava flow. All textural, petrological, and chemical analyses were carried out at the Laboratoire Magmas et Volcans (LMV, Université Clermont-Auvergne, France). Analyses at LMV benefitted from the help of Mhammed Benbakkar, Christophe Constantin, Claire Fonquernie, and Krzysztof Suchorski. Hugh Tuffen and Jonathan Fink provided helpful comments on an early version of the manuscript. We thank the reviewers, Liam Bullock and Steve Anderson, as well as the associate editor for insightful, constructive, and helpful comments that improved the focus of this work. This research was financed by the Agence Nationale de la Recherche through project LAVA (program: DS0902 2016; project: ANR-16 CE39-0009). This is Laboratory of Excellence ClerVolc contribution no. 563 and ANR-LAVA contribution 24.

REFERENCES CITED

Akkoyun, M., Majesté, J.-C., and Bascou, J., 2013, Using the anisotropy of magnetic susceptibility to infer flow-induced orientation of anisotropic particles: Feasibility and sensitivity: Rheologica Acta, v. 52, p. 49–57, https://doi.org/10.1007/s00397-012-0670-6.

Allen, J.E., 1936, Structures in the dacitic flows at Crater Lake, Oregon: The Journal of Geology, v. 44, p. 737–744, https://doi.org/10.1086/624474.

Anderson, S.W., and Fink, J.H., 1989, Hydrogen isotopic evidence for extrusion mechanisms of the Mount St. Helens dome: Nature, v. 341, p. 521–523, https://doi.org/10.1038/341521a0.

Anderson, S.W., and Fink, J.H., 1992, Crease structures: Indicators of emplacement rates and surface stress regimes of lava flows: Geological Society of America Bulletin, v. 104, p. 615–625, https://doi.org/10.1130/0016-7606(1992)104<0615:CSIOER>2.3.CO;2.

Anderson, S.W., Fink, J.H., and Rose, W.I., 1995, Mount St. Helens and Santiaguito lava domes: The effect of short-term eruption rate on surface texture and degassing processes: Journal of Volcanology and Geothermal Research, v. 69, no. 1–2, p. 105–116, https://doi.org/10.1016/0377-0273(95)00022-4.

Anderson, S.W., Stofan, E.R., Plaut, J.J., and Crown, D.A., 1998, Block size distributions on silicic lava flow surfaces: Implications for emplacement conditions: Geological Society of America Bulletin, v. 110, no. 10, p. 1258–1267, https://doi.org/10.1130/0016-7606(1998)110<1258:BSDOSL>2.3.CO;2.

Auer, A., Belousov, A., and Belousova, M., 2018, Deposits, petrology and mechanism of the 2010–2013 eruption of Kizimen volcano in Kamchatka, Russia: Bulletin of Volcanology, v. 80, https://doi.org/10.1007/s00445-018-1199-z.

Barnes, H.A., 1999, The yield stress—a review or 'παντα ρει'—everything flows?: Journal of Non-Newtonian Fluid Mechanics, v. 81, p. 133–178, https://doi.org/10.1016/S0377-0257(98)00094-9.

Bascou, J., Camps, P., and Marie Dautria, J., 2005, Magnetic versus crystallographic fabrics in a basaltic lava flow: Journal of Volcanology and Geothermal Research, v. 145, p. 119–135, https://doi.org/10.1016/j.jvolgeores.2005.01.007.

Benn, D.I., and Evans, D.J.A., 2010, Glaciers and Glaciation: London, Hodder Education, 820 p.

Blake, S., 1990, Viscoplastic models of lava domes, *in* Fink, J.H., Johnson, R.W., Mahood, G.A., and Scarpa, R. eds., Lava Flows and Domes: Berlin, Heidelberg, Springer, IAVCEI Proceedings in Volcanology, v. 2, p. 88–126, https://doi.org/10.1007/978-3-642-74379-5_5.

Bluth, G.J.S., and Rose, W.I., 2004, Observations of eruptive activity at Santiaguito volcano, Guatemala: Journal of Volcanology and Geothermal Research, v. 136, p. 297–302, https://doi.org/10.1016/j.jvolgeores.2004.06.001.

Boiron, T., Bascou, J., Camps, P., Ferré, E.C., Maurice, C., Guy, B., Gerbe, M.-C., and Launeau, P., 2013, Internal structure of basalt flows: Insights from magnetic and crystallographic fabrics of the La Palisse volcanics, French Massif Central: Geophysical Journal International, v. 193, p. 585–602, https://doi.org/10.1093/gji/ggs115.

Borradaile, G., 2003, Statistics of Earth Science Data: Berlin, Heidelberg, Springer, https://doi.org/10.1007/978-3-662-05223-5.

Brousse, R., and Tempier, P., 1981, Carte géologique de la France, feuille Bourg-Lastic (716): Orléans, Bureau de recherches géologiques et minières, échelle 1:50,000.

Brousse, R., Tempier, P., Rançon, J.P., and Veyret-Mekdjian, Y., 1989, Notice explicative, carte géologique de la France, feuille Bourg-Lastic (716): Orléans, Bureau de recherches géologiques et minières, échelle 1:50,000.

Buckland, H.M., Eychenne, J., Rust, A.C., and Cashman, K.V., 2018, Relating the physical properties of volcanic rocks to the characteristics of ash generated by experimental abrasion: Journal of Volcanology and Geothermal Research, v. 349, p. 335–350, https://doi.org/10.1016/j.jvolgeores.2017.11.017.

Bullock, L.A., Gertisser, R., and O'Driscoll, B., 2018, Emplacement of the Rocche Rosse rhyolite lava flow (Lipari, Aeolian Islands): Bulletin of Volcanology, v. 80, https://doi.org/10.1007/s00445-018-1222-4.

Bulmer, M.H., Glaze, L.S., Anderson, S., and Shockey, K.M., 2005, Distinguishing between primary and secondary emplacement events of blocky volcanic deposits using rock size distributions: Journal of Geophysical Research: Solid Earth, v. 110, p. B01201, https://doi.org/10.1029/2003JB002841.

Caballero-Miranda, C.I., Alva-Valdivia, L.M., González-Rangel, J.A., Gogitchaishvili, A., Urrutia-Fucugauchi, J., and Kontny, A., 2016, Vertical AMS variation within basalt flow profiles from the Xitle volcano (Mexico) as indicator of heterogeneous strain in lava flows: Journal of Volcanology and Geothermal Research, v. 311, p. 9–28, https://doi.org/10.1016/j.jvolgeores.2016.01.003.

Cañón-Tapia, E., 2004, Anisotropy of magnetic susceptibility of lava flows and dikes: A historical account, *in* Martín-Hernández, F., Lüneberg, C.M., Aubourg, C., and Jackson, M., eds., Magnetic Fabric: Methods and Applications: Geological Society, London, Special Publications, v. 238, p. 205–225, https://doi.org/10.1144/GSL.SP.2004.238.01.14.

Cantagrel, J.-M., and Baubron, J.-C., 1983, Chronologie des éruptions dans le massif volcanique des Monts Dore (Méthode potassium-argon). Implications volcanologiques: Géologie de la France, p. 123–142.

Carr, B.B., Clarke, A.B., Vanderkluysen, L., and Arrowsmith, J.R., 2018, Mechanisms of lava flow emplacement during an effusive eruption of Sinabung Volcano (Sumatra, Indonesia): Journal of Volcanology and Geothermal Research, v. 382, p. 137-148, https://doi.org/10.1016/j.jvolgeores.2018.03.002.

Cas, R.A.F., and Wright, J.V., 1987, Volcanic Successions, Modern and Ancient: Chapman & Hall, 550 p., https://doi.org/10.1007/978-94-009-3167-1.

Cashman, K.V., Thornber, C.R., and Pallister, J.S., 2008, From dome to dust: Shallow crystallization and fragmentation of conduit magma during the 2004–2006 dome extrusion of Mount St. Helens, Washington, *in* Sherrod, D.R., Scott, W.E., and Stauffer, P.H., eds., A Volcano Rekindled: The Renewed Eruption of Mount St. Helens, 2004–2006: U.S. Geological Survey Professional Paper 1750, p. 387–413, https://doi.org/10.3133/pp175019.

Castro, J., and Cashman, K.V., 1999, Constraints on rheology of obsidian lavas based on mesoscopic folds: Journal of Structural Geology, v. 21, p. 807–819, https://doi.org/10.1016/S0191-8141(99)00070-X.

Castro, J., Manga, M., and Cashman, K., 2002, Dynamics of obsidian flows inferred from microstructures: Insights from microlite preferred orientations: Earth and Planetary Science Letters, v. 199, p. 211–226, https://doi.org/10.1016/S0012-821X(02)00559-9.

Castruccio, A., Rust, A.C., and Sparks, R.S.J., 2013, Evolution of crust- and core-dominated lava flows using scaling analysis: Bulletin of Volcanology, v. 75, 681, https://doi.org/10.1007/s00445-012-0681-2.

Chamina, 2003, Le volcanisme en Auvergne: Clermont-Ferrand, Chamina, Découverte du patrimoine, 143 p.

Chevrel, M.O., Platz, T., Hauber, E., Baratoux, D., Lavallée, Y., and Dingwell, D.B., 2013, Lava flow rheology: A comparison of morphological and petrological methods: Earth and Planetary Science Letters, v. 384, p. 109–120, https://doi.org/10.1016/j.epsl.2013.09.022.

Chevrel, M.O., Siebe, C., Guilbaud, M.N., and Salinas, S., 2016a, The AD 1250 El Metate shield volcano (Michoacán): Mexico's most voluminous Holocene eruption and its significance for archaeology and hazards: The Holocene, v. 26, no. 3, p. 471–488, https://doi.org/10.1177/0959683615609757.

Chevrel, M.O., Guilbaud, M.-N., and Siebe, C., 2016b, The ∼AD 1250 effusive eruption of El Metate shield volcano (Michoacán, Mexico): Magma source, crustal storage, eruptive dynamics, and lava rheology: Bulletin of Volcanology, v. 78, https://doi.org/10.1007/s00445-016-1020-9.

Christiansen, R.L., and Lipman, P.W., 1966, Emplacement and thermal history of a rhyolite lava flow near Fortymile Canyon, Southern Nevada: Geological Society of America Bulletin, v. 77, p. 671, https://doi.org/10.1130/0016-7606(1966)77[671:EATHOA]2.0.CO;2.

Cigolini, C., Borgia, A., and Casertano, L., 1984, Intra-crater activity, aa-block lava, viscosity and flow dynamics: Arenal Volcano, Costa Rica: Journal of Volcanology and Geothermal Research, v. 20, p. 155–176, https://doi.org/10.1016/0377-0273(84)90072-6.

Cioni, R., and Funedda, A., 2005, Structural geology of crystal-rich, silicic lava flows: A case study from San Pietro Island (Sardinia, Italy), *in* Mango, M., and Ventura, G., eds., Kinematics and Dynamics of Lava Flows: Geological Society of America Special Paper 396, p. 1–14, https://doi.org/10.1130/0-8137-2396-5.1.

Cuffey, K., and Paterson, W.S.B., 2010, The Physics of Glaciers: Oxford, Butterworth-Heinemann/Elsevier.

Dadd, K.A., 1992, Structures within large volume rhyolite lava flows of the Devonian Comerong volcanics, southeastern Australia, and the Pleistocene Ngongotaha lava dome, New Zealand: Journal of Volcanology and Geothermal Research, v. 54, p. 33–51, https://doi.org/10.1016/0377-0273(92)90113-R.

Degraff, J.M., and Aydin, A., 1987, Surface morphology of columnar joints and its significance to mechanics and direction of joint growth: Geological Society of America Bulletin, v. 99, p. 605–617, https://doi.org/10.1130/0016-7606(1987)99<605:SMOCJA>2.0.CO;2.

Delabroy, C., Derouard, H., Huon, C., and Rothan, É., 2019, Explorer la région Auvergne: Paris, Lonely Planet.

de Lima, E.F., Waichel, B.L., Rossetti, L.D.M.M., Sommer, C.A., and Simões, M.S., 2018, Feeder systems of acidic lava flows from the Paraná-Etendeka Igneous Province in southern Brazil and their implications for eruption style: Journal of South American Earth Sciences, v. 81, p. 1–9, https://doi.org/10.1016/j.jsames.2017.11.004.

De Silva, S.L., Self, S., Francis, P.W., Drake, R.E., and Carlos, R.R., 1994, Effusive silicic volcanism in the Central Andes: The Chao dacite and other young lavas of the Altiplano–Puna Volcanic Complex: Journal of Geophysical Research: Solid Earth, v. 99, B9, p. 17805–17825, https://doi.org/10.1029/94JB00652.

Drake, M.J., and Weill, D.F., 1975, Partition of Sr, Ba, Ca, Y, Eu^{2+}, Eu^{3+}, and other REE between plagioclase feldspar and magmatic liquid: An experimental study: Geochimica et Cosmochimica Acta, v. 39, p. 689–712, https://doi.org/10.1016/0016-7037(75)90011-3.

Eichelberger, J.C., Carrigan, C.R., Westrich, H.R., and Price, R.H., 1986, Non-explosive silicic volcanism: Nature, v. 323, p. 598–602, https://doi.org/10.1038/323598a0.

Escobar-Wolf, R., Matias Gomez, R.O., and Rose, W.I., 2010, Geologic map of Santiaguito Volcano, Guatemala: Geological Society of America Digital Map and Chart Series 8.

Etlicher, B., and De Goër De Hervé, A., 1988, La déglaciation würmienne dans le Massif Central français, le point des travaux récents / The Würmian déglaciation in the French Massif-Central, review of recent works: Bulletin de l'Association française pour l'étude du quaternaire, v. 25, p. 103–110, https://doi.org/10.3406/quate.1988.1871.

Fédération française de la randonnée pédestre, 2018, Volcans et lacs d'Auvergne: Paris, FFRandonnée.

Fédération des Parcs, 2021, Carte des 58 Parcs: Map sheet, https://www.parcs-naturels-regionaux.fr/mediatheque/ressources/carte-des-58-parcs-septembre-2021.

Finch, R.H., 1933, Block lava: The Journal of Geology, v. 41, p. 769–770, https://doi.org/10.1086/624096.

Fink, J.H., 1983, Structure and emplacement of a rhyolitic obsidian flow: Little Glass Mountain, Medicine Lake Highland, northern California: Geological Society of America Bulletin, v. 94, p. 362, https://doi.org/10.1130/0016-7606(1983)94<362:SAEOAR>2.0.CO;2.

Fink, J.H., and Manley, C.R., 1987, Origin of pumiceous and glassy textures in rhyolite flows and domes, *in* Fink, J.H., The Emplacement of Silicic Domes and Lava Flows: Geological Society of America Special Paper 212, p. 77–88, https://doi.org/10.1130/SPE212-p77.

Fischer, U.H., and Clarke, G.K.C., 1994, Ploughing of subglacial sediment: Journal of Glaciology, v. 40, p. 97–106, https://doi.org/10.1017/S0022143000003853.

Flint, R.F., Sanders, J.E., and Rodgers, J., 1960, Diamictite, a substitute term for symmictite: Geological Society of America Bulletin, v. 71, no. 12, p. 1809–1810, https://doi.org/10.1130/0016-7606(1960)71[1809:DASTFS]2.0.CO;2.

Folk, R.L., and Ward, W.C., 1957, Brazos River bar: A study in the significance of grain size parameters: Journal of Sedimentary Petrology, v. 27, p. 3–26, https://doi.org/10.1306/74D70646-2B21-11D7-8648000102C1865D.

Forbes, J.D., 1846, Illustrations of the viscous theory of glacier motion.—Part I. Containing experiments on the flow of plastic bodies, and observations on the phenomena of lava streams: Philosophical Transactions of the Royal Society of London, v. 136, p. 143–155, https://doi.org/10.1098/rstl.1846.0013.

Ghiorso, M.S., and Evans, B.W., 2008, Thermodynamics of rhombohedral oxide solid solutions and a revision of the FE-TI two-oxide geothermometer and oxygen-barometer: American Journal of Science, v. 308, p. 957–1039, https://doi.org/10.2475/09.2008.01.

Giordano, D., Russell, J.K., and Dingwell, D.B., 2008, Viscosity of magmatic liquids: A model: Earth and Planetary Science Letters, v. 271, p. 123–134, https://doi.org/10.1016/j.epsl.2008.03.038.

Glangeaud, P., 1919, Le groupe volcanique adventif ou de superposition du Massif des Monts Dore: Comptes Rendus Hebdomadaires des Séances de l'Académie des Sciences, v. 168, p. 1157–1159.

Golombek, M.P., Haldemann, A.F.C., Forsberg-Taylor, N.K., DiMaggio, E.N., Schroeder, R.D., Jakosky, B.M., Mellon, M.T., and Matijevic, J.R., 2003, Rock size-frequency distributions on Mars and implications for Mars Exploration Rover landing safety and operations: Journal of Geophysical Research: Planets, v. 108, E12, https://doi.org/10.1029/2002JE002035.

Gonnermann, H.M., and Manga, M., 2005, Flow banding in obsidian: A record of evolving textural heterogeneity during magma deformation: Earth and Planetary Science Letters, v. 236, p. 135–147, https://doi.org/10.1016/j.epsl.2005.04.031.

Gourgaud, A., 1985, Mélanges de magmas dans les séries alcalines et calco-alcalines: Leur rôle dans le genèse des laves intermédiaires et leur influence sur les mécanismes éruptifs: Clermont II.

Gourgaud, A., and Maury, R.C., 1984, Magma mixing in alkaline series: An example from Sancy volcano (Mont-Dore, Massif Central, France): Bulletin Volcanologique, v. 47, p. 827–847, https://doi.org/10.1007/BF01952346.

Graveline, N., 2002, Known & Little-Known Volcanoes of the Massif Central: Beaumont, France, Debaisieux.

Greeley, R., and Fagents, S.A., 2001, Icelandic pseudocraters as analogs to some volcanic cones on Mars: Journal of Geophysical Research: Planets, v. 106, p. 20,527–20,546, https://doi.org/10.1029/2000JE001378.

Gregg, T.K.P., and Fink, J.H., 2000, A laboratory investigation into the effects of slope on lava flow morphology: Journal of Volcanology and Geothermal Research, v. 96, no. 3–4, p. 145–159.

Gurioli, L., Zanella, E., Pareschi, M.T., and Lanza, R., 2007, Influences of urban fabric on pyroclastic density currents at Pompeii (Italy): 1. Flow direction and deposition: Journal of Geophysical Research: Solid Earth, v. 112, https://doi.org/10.1029/2006JB004444.

Hamilton, C.W., Thordarson, T., and Fagents, S.A., 2010, Explosive lava–water interactions I: Architecture and emplacement chronology of volcanic rootless cone groups in the 1783–1784 Laki lava flow, Iceland: Bulletin of Volcanology v. 72, p. 449–467, https://doi.org/10.1007/s00445-009-0330-6.

Hargraves, R.B., Johnson, D., and Chan, C.Y., 1991, Distribution anisotropy: The cause of AMS in igneous rocks?: Geophysical Research Letters, v. 18, p. 2193–2196, https://doi.org/10.1029/91GL01777.

Harris, A.J.L., Flynn, L.P., Matías, O., and Rose, W.I., 2002, The thermal stealth flows of Santiaguito dome, Guatemala: Implications for the cooling and emplacement of dacitic block-lava flows: Geological Society of America Bulletin, v. 114, p. 533–546, https://doi.org/10.1130/0016-7606(2002)114<0533:TTSFOS>2.0.CO;2.

Harris, A.J.L., Rose, W.I., and Flynn, L.P., 2003, Temporal trends in lava dome extrusion at Santiaguito 1922–2000: Bulletin of Volcanology, v. 65, p. 77–89, https://doi.org/10.1007/s00445-002-0243-0.

Harris, A.J.L., Flynn, L.P., Matias, O., Rose, W.I., and Cornejo, J., 2004, The evolution of an active silicic lava flow field: An ETM+ perspective: Journal of Volcanology and Geothermal Research, v. 135, p. 147–168, https://doi.org/10.1016/j.jvolgeores.2003.12.011.

Heilbronner, R., and Barrett, S., 2014, Image Analysis in Earth Sciences: Berlin Heidelberg, Springer-Verlag, https://doi.org/10.1007/978-3-642-10343-8.

Henry, C.D., and Wolff, J.A., 1992, Distinguishing strongly rheomorphic tuffs from extensive silicic lavas: Bulletin of Volcanology, v. 54, p. 171–186, https://doi.org/10.1007/BF00278387.

Hillhouse, J.W., and Wells, R.E., 1991, Magnetic fabric, flow directions, and source area of the Lower Miocene Peach Springs Tuff in Arizona, California, and Nevada: Journal of Geophysical Research: Solid Earth, v. 96, p. 12,443–12,460, https://doi.org/10.1029/90JB02257.

Hrouda, F., 1982, Magnetic anisotropy of rocks and its application in geology and geophysics: Geophysical Surveys, v. 5, p. 37–82, https://doi.org/10.1007/BF01450244.

Iezzi, G., and Ventura, G., 2000, Kinematics of lava flows based on fold analysis: Geophysical Research Letters, v. 27, no. 8, p. 1227–1230, https://doi.org/10.1029/1999GL011279.

Institut national de l'information géographique et forestière, 2016, Massif du Sancy, PNR des Volcans d'Auvergne: IGN.

Jones, T.J., McNamara, K., Eychenne, J., Rust, A.C., Cashman, K.V., Scheu, B., and Edwards, R., 2016, Primary and secondary fragmentation of crystal-bearing intermediate magma: Journal of Volcanology and Geothermal Research, v. 327, p. 70–83, https://doi.org/10.1016/j.jvolgeores.2016.06.022.

Jung, J., 1946, Géologie de l'Auvergne et de ses confins bourbonnais et limousins: Impr. Nationale, Mémoires pour servir à l'explication de la carte géologique détaillée de la France, 372 p.

Kalmar, P., and Chassain, D., 2012, Quatre cents cascades dans le Puy-de-Dôme: Le Mont-Dore, Crebu Nigo, 232 p.

Kaminski, E., and Jaupart, C., 1998, The size distribution of pyroclasts and the fragmentation sequence in explosive volcanic eruptions: Journal of Geophysical Research: Solid Earth, v. 103, p. 29,759–29,779, https://doi.org/10.1029/98JB02795.

Kendrick, J.E., Lavallée, Y., Ferk, A., Perugini, D., Leonhardt, R., and Dingwell, D.B., 2012, Extreme frictional processes in the volcanic conduit of Mount St. Helens (USA) during the 2004–2008 eruption: Journal of Structural Geology, v. 38, p. 61–76, https://doi.org/10.1016/j.jsg.2011.10.003.

Khan, M.A., 1962, The anisotropy of magnetic susceptibility of some igneous and metamorphic rocks: Journal of Geophysical Research, v. 67, p. 2873–2885, https://doi.org/10.1029/JZ067i007p02873.

Krieger, I.M., and Dougherty, T.J., 1959, A mechanism for non-Newtonian flow in Suspensions of rigid spheres: Transactions of the Society of Rheology, v. 3, p. 137–152, https://doi.org/10.1122/1.548848.

Kudo, A.M., and Weill, D.F., 1970, An igneous plagioclase thermometer: Contributions to Mineralogy and Petrology, v. 25, p. 52–65, https://doi.org/10.1007/BF00383062.

Kueppers, U., Perugini, D., and Dingwell, D., 2006, "Explosive energy" during volcanic eruptions from fractal analysis of pyroclasts: Earth and Planetary Science Letters, v. 248, p. 800–807, https://doi.org/10.1016/j.epsl.2006.06.033.

Lara, L.E., Naranjo, J.A., and Moreno, H., 2004, Rhyodacitic fissure eruption in Southern Andes (Cordón Caulle; 40.5°S) after the 1960 (Mw:9.5) Chilean earthquake: A structural interpretation: Journal of Volcanology and Geothermal Research, v. 138, p. 127–138, https://doi.org/10.1016/j.jvolgeores.2004.06.009.

Latutrie, B., Harris, A., Médard, E., and Gurioli, L., 2017, Eruption and emplacement dynamics of a thick trachytic lava flow of the Sancy volcano (France): Bulletin of Volcanology, v. 79, https://doi.org/10.1007/s00445-016-1084-6.

Lawson, W.J., Sharp, M.J., and Hambrey, M.J., 1994, The structural geology of a surge-type glacier: Journal of Structural Geology, v. 16, no. 10, p. 1447–1462, https://doi.org/10.1016/0191-8141(94)90008-6.

Le Maitre, R.W., Streckeisen, A., Zanettin, B., Le Bas, M.J., Bonin, B., and Bateman, P., eds., 2002, Igneous rocks: A classification and glossary of terms: Cambridge, Cambridge University Press, https://doi.org/10.1017/CBO9780511535581.

Lecoq, H., and Bouillet, J.-B., 1830, Vues et coupes des principales formations géologiques du Département du Puy-de-Dome: Clermont-Ferrand, France, Bouillet, 266 p.

Liu, E., Cashman, K., and Rust, A., 2015, Optimising shape analysis to quantify volcanic ash morphology: GeoResJ, v. 8, p. 14–30, https://doi.org/10.1016/j.grj.2015.09.001.

Loock, S., Diot, H., Van Wyk de Vries, B., Launeau, P., Merle, O., Vadeboin, F., and Petronis, M.S., 2008, Lava flow internal structure found from AMS and textural data: An example in methodology from the Chaîne des Puys, France: Journal of Volcanology and Geothermal Research, v. 177, p. 1092–1104, https://doi.org/10.1016/j.jvolgeores.2008.08.017.

Macdonald, G.A., 1953, Pahoehoe, aa, and block lava: American Journal of Science, v. 251, p. 169–191, https://doi.org/10.2475/ajs.251.3.169.

Magnall, N., James, M.R., Tuffen, H., and Vye-Brown, C., 2017, Emplacing a cooling-limited rhyolite lava flow: Similarities with basaltic lava flows: Frontiers of Earth Science, v. 5, https://doi.org/10.3389/feart.2017.00044.

Mallet, R., 1875, XVI. On the origin and mechanism of production of the prismatic (or columnar) structure of basalt: The London, Edinburgh and Dublin Philosophical Magazine and Journal of Science, v. 50, p. 122–135, https://doi.org/10.1080/14786447508641268.

Manley, C.R., 1992, Extended cooling and viscous flow of large, hot rhyolite lavas: Implications of numerical modeling results: Journal of Volcanology and Geothermal Research, v. 53, p. 27–46, https://doi.org/10.1016/0377-0273(92)90072-L.

Manley, C.R., 1996, Physical volcanology of a voluminous rhyolite lava flow: The Badlands lava, Owyhee Plateau, Southern Idaho: Journal of Volcanology and Geothermal Research, v. 71, p. 129–153, https://doi.org/10.1016/0377-0273(95)00066-6.

Manley, C.R., and Fink, J.H., 1987, Internal textures of rhyolite flows as revealed by research drilling: Geology, v. 15, p. 549–552, https://doi.org/10.1130/0091-7613(1987)15<549:ITORFA>2.0.CO;2.

Menzies, J., 2009, Diamicton, *in* Gornitz, V., ed., Encyclopedia of Paleoclimatology and Ancient Environments: Dordrecht, Springer, p. 278–279, https://doi.org/10.1007/978-1-4020-4411-3_68.

Merle, O., 1998, Internal strain within lava flows from analogue modelling: Journal of Volcanology and Geothermal Research, v. 81, p. 189–206, https://doi.org/10.1016/S0377-0273(98)00009-2.

Michelin, 2019, Guide Vert Auvergne: Paris, Michelin, 597 p.

Nakada, S., et al., 2019, Growth process of the lava dome/flow complex at Sinabung Volcano during 2013–2016: Journal of Volcanology and Geothermal Research, v. 382, p. 120–136, https://doi.org/10.1016/j.jvolgeores.2017.06.012.

Nielson, D.L., and Sibbett, B.S., 1996, Geology of ascension Island, South Atlantic Ocean: Geothermics, v. 25, p. 427–448, https://doi.org/10.1016/0375-6505(96)00018-1.

Nomade, S., Scaillet, S., Pastre, J.-F., and Nehlig, P., 2012, Pyroclastic chronology of the Sancy stratovolcano (Mont-Dore, French Massif Central): New high-precision $^{40}Ar/^{39}Ar$ constraints: Journal of Volcanology and Geothermal Research, v. 225–226, p. 1–12, https://doi.org/10.1016/j.jvolgeores.2012.02.006.

Nomade, S., Pastre, J.-F., Nehlig, P., Guillou, H., Scao, V., and Scaillet, S., 2014, Tephrochronology of the Mont-Dore volcanic Massif (Massif Central, France): new $^{40}Ar/^{39}Ar$ constraints on the late Pliocene and early Pleistocene activity: Bulletin of Volcanology, v. 76, 798, https://doi.org/10.1007/s00445-014-0798-6.

Pallister, J.S., Thornber, C.R., Cashman, K.V., Clynne, M.A., Lowers, H.A., Mandeville, C.W., Brownfield, I.K., and Meeker, G.P., 2008, Petrology of the 2004–2006 Mount St. Helens lave dome—implications for magmatic plumbing and eruption triggering, *in* Sherrod, D.R., Scott, W.E., and Stauffer, P.H., eds., A Volcano Rekindled the Renewed Eruption of Mount St. Helens 2004–2006: U.S. Geological Survey Professional Paper 1750, p. 647–702.

Pallister, J.S., Cashman, K.V., Hagstrum, J.T., Beeler, N.M., Moran, S.C., and Denlinger, R.P., 2013, Faulting within the Mount St. Helens conduit and implications for volcanic earthquakes: Geological Society of America Bulletin, v. 125, p. 359–376, https://doi.org/10.1130/B30716.1.

Powell, R., and Powell, M., 1977, Geothermometry and oxygen barometry using coexisting iron-titanium oxides: A reappraisal: Mineralogical Magazine, v. 41, p. 257–263, https://doi.org/10.1180/minmag.1977.041.318.14.

Putirka, K.D., 2008, Thermometers and barometers for volcanic systems: Reviews in Mineralogy and Geochemistry, v. 69, p. 61–120, https://doi.org/10.2138/rmg.2008.69.3.

Ramírez-Uribe, I., Siebe, C., Chevrel, M.O., and Fisher, C.T., 2021, Rancho Seco monogenetic volcano (Michoacán, Mexico): Petrogenesis and lava flow emplacement based on LiDAR images: Journal of Volcanology and Geothermal Research, v. 411, https://doi.org/10.1016/j.jvolgeores.2020.107169.

Ramírez-Uribe, I., Siebe, C., Chevrel, M.O., Ferrés, D., and Salinas, S., 2022, The late Holocene Nealtican lava-flow field from Popocatépetl volcano: Emplacement dynamics and implications for future hazard scenarios and archaeology: Geological Society of America Bulletin, https://doi.org/10.1130/B36173.1.

Reyes-Guzmán, N., Siebe, C., Chevrel, M.O., and Pereira, P., 2021, Late Holocene Malpaís de Zacapu (Michoacán, Mexico) andesitic lava flows: Rheology and eruption properties based on LiDAR image: Bulletin of Volcanology, v. 83, p. 28, https://doi.org/10.1007/s00445-021-01449-0.

Rhodes, E., Kennedy, B.M., Lavallée, Y., Hornby, A., Edwards, M., and Chigna, G., 2018, Textural insights into the evolving lava dome cycles at Santiaguito lava dome, Guatemala: Frontiers in Earth Science v. 6, no. 30, https://doi.org/10.3389/feart.2018.00030.

Richet, P., 2003, Guide des volcans de France: Paris, Belin, Guides savants, 427 p.

Rochette, P., Jackson, M., and Aubourg, C., 1992, Rock magnetism and the interpretation of anisotropy of magnetic susceptibility: Reviews of Geophysics, v. 30, p. 209–226, https://doi.org/10.1029/92RG00733.

Rose, W.I., 1987, Volcanic activity at Santiaguito volcano, 1976–1984, *in* Fink, J.H., ed., The Emplacement of Silicic Domes and Lava Flows: Geological Society of America Special Paper 212, p. 17–28, https://doi.org/10.1130/SPE212-p17.

Sahetapy-Engel, S.T., Harris, A.J.L., and Marchetti, E., 2008, Thermal, seismic and infrasound observations of persistent explosive activity and conduit dynamics at Santiaguito lava dome, Guatemala: Journal of Volcanology and Geothermal Research, v. 173, p. 1–14, https://doi.org/10.1016/j.jvolgeores.2007.11.026.

Schulmann, K., and Ježek, J., 2012, Some remarks on fabric overprints and constrictional AMS fabrics in igneous rocks: International Journal of Earth Sciences, v. 101, p. 705–714, https://doi.org/10.1007/s00531-011-0681-z.

Scrope, G.P., 1827, Memoir on the Geology of Central France, Including the Volcanic Formations of Auvergne, the Velay, and the Vivarais: London, Rees, Orme, Brown, and Green, 182 p., https://books.google.fr/books?id=e2xdAAAAcAAJ.

Self, S., and Gunn, B.M., 1976, Petrology, volume and age relations of alkaline and saturated peralkaline volcanics from Terceira, Azores: Contributions to Mineralogy and Petrology, v. 54, p. 293–313, https://doi.org/10.1007/BF00389409.

Siebe, C., Guilbaud, M.-N., Salinas, S., Kshirsagar, P., Chevrel, M.O., De la Fuente, J.R., Hernández-Jiménez, A., and Godínez, L., 2014, Monogenetic volcanism of the Michoacán-Guanajuato volcanic field: Maar craters of the Zacapu basin and domes, shields, and scoria cones of the Tarascan highland (Paracho-Paricutin region), *in* Field Guide, Pre-Meeting Fieldtrip for the 5th International Maar Conference (5IMC-IAVCEI): National Autonomous University of Mexico Center of Geosciences, 33 p.

Smith, J.V., 1996, Ductile-brittle transition structures in the basal shear zone of a rhyolite lava flow, eastern Australia: Journal of Volcanology and Geothermal Research, v. 72, p. 217–223, https://doi.org/10.1016/0377-0273(96)00009-1.

Smith, J.V., and Houston, E.C., 1994, Folds produced by gravity spreading of a banded rhyolite lava flow: Journal of Volcanology and Geothermal Research, v. 63, p. 89–94, https://doi.org/10.1016/0377-0273(94)90019-1.

Smith, J.V., Yamauchi, S., and Miyake, Y., 1993, Micro shear zones in a Miocene submarine dacite dome of southwest Japan: Bulletin of Volcanology v. 55, p. 438–442, https://doi.org/10.1007/BF00302003.

Tarling, D.H., and Hrouda, F., 1993, The magnetic anisotropy of rocks: London, Chapman & Hall, 217 p.

Taylor, B., Eichelberger, J., and Westrich, H., 1983, Hydrogen isotopic evidence of rhyolitic magma degassing during shallow intrusion and eruption: Nature, v. 306, p. 541–545, https://doi.org/10.1038/306541a0.

Thivet, S., Gurioli, L., Di Muro, A., Eychenne, J., Besson, P., and Nedelec, J.-M., 2020, Variability of ash deposits at Piton de la Fournaise (La Reunion Island): Insights into fragmentation processes at basaltic shield volcanoes: Bulletin of Volcanology, v. 82, p. 63, https://doi.org/10.1007/s00445-020-01398-0.

Thorarinsson, S., 1953a, The crater groups in Iceland: Bulletin of Volcanology, v. 14, p. 3–44, https://doi.org/10.1007/BF02596003.

Thorarinsson, S., 1953b, Ogives in lava streams: Journal of Glaciology, v. 2, p. 295, https://doi.org/10.1017/S002214300002551X.

Tomkeieff, S.I., 1940, The basalt lavas of the Giant's Causeway district of Northern Ireland: Bulletin of Volcanology, v. 6, p. 89–143, https://doi.org/10.1007/BF02994875.

Tuffen, H., and Dingwell, D., 2005, Fault textures in volcanic conduits: Evidence for seismic trigger mechanisms during silicic eruptions: Bulletin of Volcanology, v. 67, p. 370–387, https://doi.org/10.1007/s00445-004-0383-5.

Tuffen, H., Dingwell, D.B., and Pinkerton, H., 2003, Repeated fracture and healing of silicic magma generate flow banding and earthquakes?: Geology, v. 31, p. 1089–1092, https://doi.org/10.1130/G19777.1.

Tuffen, H., James, M.R., Castro, J.M., and Schipper, C.I., 2013, Exceptional mobility of an advancing rhyolitic obsidian flow at Cordón Caulle volcano in Chile: Nature Communications, v. 4, 2709, https://doi.org/10.1038/ncomms3709.

Turcotte, D.L., 1986, Fractals and fragmentation: Journal of Geophysical Research: Solid Earth, v. 91, p. 1921–1926, https://doi.org/10.1029/JB091iB02p01921.

Veyret, Y., 1978, Modèles et formations d'origine glaciaire dans le Massif Central français: Problèmes de distribution et de limites dans un milieu de moyenne montagne [Doctorat d'État]: Paris, Université Paris 1 Panthéon-Sorbonne.

Wadge, G., and Lopes, R.M.C., 1991, The lobes of lava flows on Earth and Olympus Mons, Mars: Bulletin of Volcanology, v. 54, p. 10–24, https://doi.org/10.1007/BF00278203.

Walker, G.P.L., 1973, Lengths of lava flows: Philosophical Transactions of the Royal Society of London, v. 274, p. 107–118.

Wanless, V.D., Perfit, M.R., Ridley, W.I., and Klein, E., 2010, Dacite petrogenesis on mid-ocean ridges: Evidence for oceanic crustal melting and assimilation: Journal of Petrology, v. 51, p. 2377–2410, https://doi.org/10.1093/petrology/egq056.

Wiesmaier, S., Troll, V.R., Rodríguez-Badiola, E., and Carracedo, J.C., 2013, Timing, distribution and petrological evolution of the Teide-Pico Viejo volcanic complex, *in* Carracedo, J.C., and Troll, V.R., eds., Teide Volcano: Berlin, Heidelberg, Springer, p. 155–172, https://doi.org/10.1007/978-3-642-25893-0_9.

Wilson, M., 1989, Igneous Petrogenesis: London, Chapman & Hall, https://doi.org/10.1007/978-1-4020-6788-4.

Závada, P., Kratinová, Z., Kusbach, V., and Schulmann, K., 2009, Internal fabric development in complex lava domes: Tectonophysics, v. 466, p. 101–113, https://doi.org/10.1016/j.tecto.2008.07.005.

Science Editor: Brad Singer
Associate Editor: Richard Waitt

Manuscript Received 9 December 2021
Revised Manuscript Received 9 July 2022
Manuscript Accepted 29 August 2022

Printed in the USA